APPLIED SCIENCES AND ENGINEERING

Structure-guided design of nucleosome-inspired nanoparticles for overcoming pulmonary barriers in fibrotic lung gene therapy

Nan Kong[1,2]†, Dinghao Chen[1,2]†, Bihan Wu[1,2], Juan Liang[1,2], Ziao Zhou[1,2], Huanfen Lu[1,2], Yaoting Li[1,2], Peng Zhang[1,2], Huayang Liu[1,2], Huaimin Wang[1,2]*

Treating pulmonary fibrosis (PF), a progressive and fatal lung disease, remains a great challenge. Here, we report a nucleosome-inspired peptide MNM designed to overcome mucus and cellular barriers, which achieved pulmonary si*TGF-β1* delivery efficiently for PF therapy. By mimicking histone-mediated DNA packaging, we engineered MNM with three functional modules: a histone-mimetic small interfering RNA (siRNA) binder, a membrane-penetrating domain, and a hydrophilic mucus-diffusing sequence. MNM integrates mucus penetration, cellular uptake, and endosomal escape into one platform, achieving highly efficient pulmonary siRNA delivery. MNM–si*TGF-β1* nanoparticles suppressed profibrotic gene expression and inflammation, which notably improved survival and reduced collagen deposition in aggressive PF models. This work establishes a biomimetic strategy to overcome complex biological barriers, advancing siRNA therapy for PF. Beyond si*TGF-β1* delivery for PF therapy, MNM's modular design is adaptable to messenger RNA, circular RNA, and other nucleic acids, offering a transformative platform for precision nanomedicine in pulmonary and systemic diseases.

INTRODUCTION

Pulmonary fibrosis (PF) is a chronic and progressive lung disease characterized by inflammatory disorders, excessive extracellular matrix deposition, and scar formation in the lung section, which impair gas exchange, leading to breathlessness and reduced quality of life (1–3). It affects approximately 5 million people worldwide, with PF having a median survival of only 3 to 5 years (4). Moreover, emerging evidence suggests that COVID-19 infections might exacerbate the risks of PF, further underscoring the urgent need for more effective and targeted therapies (5, 6). The pathological progression of PF is driven by complex cross-talk between various cell types (7). Lung injury and repair are central to this intercellular communication of transforming growth factor–β1 (*TGF-β1*), secreted by activated epithelial cells and polarized macrophages, to lastly promote fibroblast and myofibroblast activation, migration, and proliferation (8). Currently, PF has few treatments in the clinic, including immunomodulation like glucocorticoids and antifibrotic drugs pirfenidone and nintedanib, which provide limited efficacy and are associated with marked side effects (9, 10).

Gene therapy, including mRNA, CRISPR-Cas–based gene editing, and RNA interference (RNAi), holds substantial potential for the treatment of PF (11–14). RNAi-based therapies, particularly those based on small interfering RNAs (siRNAs), offer a potent strategy to target disease-driving genes at the molecular level. However, delivering siRNA to the lungs remains a formidable challenge due to extracellular and intracellular barriers (15, 16). The airway mucus layer constitutes the initial barrier for inhaled gene cargo, characterized by its sticky network with a thickness ranging from 10 to 30 μm (17). This mucus layer comprises various components, including mucins, antimicrobial molecules, cellular debris, and protective factors (18).

The O-glycosylated domains and glycans in mucin proteins confer strong negative charges and hydrophobic properties (19). Moreover, the mucus layer exhibits size exclusion effect to restrict the diffusion of large nanostructures due to its ~200 nm average pore size (20). Therefore, to minimize the interaction with mucus while enhancing overall penetration, gene cargo shall have (i) a neutrally to positively charged surface with a hydrophilic surface and (ii) a diameter smaller than the cutoff size of the mucin network (21–23). Beyond the mucus barrier, the negatively charged cell membrane barrier and lysosome trapping pose additional challenges for gene therapy. Therefore, effective delivery systems must also facilitate endosomal escape to release siRNA into the cytoplasm and achieve therapeutic effects (24). Furthermore, the powerful shear forces of nebulization pose another great challenge for inhaled gene delivery vesicles (25).

Some advances have been made in pulmonary gene delivery platforms, including lipid nanoparticles (LNPs), polymers, extracellular vesicles (EVs), and peptide-based cargos (26–30). However, recent clinical trials for PF gene therapy did not demonstrate a notable therapeutic effect, highlighting an urgent need to develop effective inhalable gene delivery systems (31, 32). Polymer-based systems, such as polyethyleneimine (PEI), offer high transfection efficiency but are associated with cytotoxicity, which limits their applicability in pulmonary disease therapy (33). In addition, effective LNP pulmonary delivery often requires extensive optimization of lipid composition, and current formulations lack structural adaptability and cell-type specificity (25, 34). Although EVs have emerged as promising candidates for pulmonary gene delivery, challenges remain in terms of scalable production and standardized quality control (27). Most existing systems are designed with single functionality, lacking biomimetic architectures that can dynamically respond to the complex pulmonary microenvironment. Notably, peptide-based gene delivery holds the potential to condense nucleic acid while resolving an aforementioned barrier, thus receive increasing attention in delivery vehicle development (35–38). Inspired by the natural self-assembly of peptides and proteins, researchers have designed a

[1]Department of Chemistry, School of Science, Westlake University, 600 Dunyu Road, Hangzhou 310030, Zhejiang, China. [2]State Key Laboratory of Gene Expression, School of Science, Westlake University, Hangzhou, Zhejiang, China.
*Corresponding author. Email: wanghuaimin@westlake.edu.cn
†These authors contributed equally to this work.

variety of biomimetic materials with tailored physicochemical and biological properties (*39–42*). In particular, peptide or protein-based bio-mimic gene delivery systems have garnered increasing attention due to their modular design and capacity for targeted delivery (*43–47*). However, many current peptide-based delivery systems are derived from cell-penetrating peptides, such as TAT and R8, which, although effective in vitro, often exhibit limited performance in vivo. Their highly positive charge makes them prone to being trapped by the mucus barrier, resulting in rapid entrapment and clearance, thereby hindering efficient pulmonary delivery (*48*).

Here, we report a structure-guided design of nucleosome-inspired peptide NPs for pulmonary siRNA delivery. Inspired by the natural architecture of nucleosomes, we developed peptide sequences that efficiently package and protect siRNA (*49, 50*). To overcome cellular barriers, we incorporated a membrane-penetrating module at the N terminus. In addition, the introduction of a hydrophilic mucus-penetrating sequence (MPS) at the C terminus facilitated diffusion through the airway mucus layer and controlled the self-assembly of peptide-siRNA NPs (Fig. 1A) (*51, 52*). Through systematic optimization, we obtained a robust delivery platform that overcomes both pulmonary and cellular barriers, enabling efficient siRNA delivery to lung tissues. We demonstrate the therapeutic potential of this platform by delivering si*TGF-β1* for treating PF, achieving substantial antifibrotic effects in preclinical models (Fig. 1B). By combining structure-guided design with modular peptide engineering, this work not only advances the field of pulmonary gene delivery but also provides a promising therapeutic strategy for treating PF.

RESULTS
Design and optimization of peptide carriers for pulmonary siRNA delivery
To address the challenges of siRNA delivery to lung tissues, we designed peptide carriers inspired by the structure of nucleosomes, which efficiently package nucleic acids (*49*). We developed nucleic acid–binding units (RFH or KFH) based on key amino acids (R, H, and K) involved in histone-DNA interactions, with phenylalanine (F) serving as an assembly unit. Furthermore, to overcome cellular barriers, we modified various membrane-penetrating sequences at the N terminus of RNA-binding sequences, incorporating different hydrophilic properties. We synthesized a combinatorial library of peptides, designated P1 to P24 (figs. S1 and S2 and table S1). Initial screening using electrophoretic gel assay revealed the RNA binding ability of peptides containing three repeated RFH units, which exhibited superior siRNA packaging efficiency compared to KFH-containing variants (fig. S3), likely due to the stronger electrostatic interactions and structural stability provided by RFH. Subsequently, flow cytometry screening revealed that the siRNA transfection rates for P9, P10, and P14 exceeded 90% (figs. S4 to S7). Representative microscopy images further demonstrated the high siRNA delivery efficiency of these peptides, with strong cytoplasmic siRNA-Cy5 signal observed in cells transfected with P9, P10, and P14 (figs. S8 to S10). These results suggest that the hydrophobic membrane–penetrating peptide sequences facilitate the overcoming of cellular barriers (Fig. 1C). However, at this concentration, P9 and P10 exhibited cytotoxicity to HBE135-E6E7 cells, showing about 80% cell viability at 16 μM. Therefore, in the first stage, we identified P14 (designated as MN, PFVYLIRFHRF-HRH) as the most efficient and least toxic siRNA delivery cargo in vitro, achieving a 98% siRNA delivery efficiency in A549 cells.

To further enhance mucus penetration, we modified the MN with hydrophilic MPSs (*53, 54*), synthesizing peptides P25 to P30 (figs. S11 and S12 and table S2). First, we conducted an electrophoretic gel assay, which demonstrated that peptides P25 to P30 were capable of encapsulating siRNA at N/P ratios ranging from 4 to 20 (fig. S13). In addition, flow cytometry screening in A549 cells demonstrated that P26, P27, and P29 achieved approximately 90 to 100% siRNA delivery efficiency (Fig. 1D and fig. S14). However, P26 and P27 exhibited high cytotoxicity in HBE (Fig. 1E). P29, designated as MNM, demonstrated high delivery efficiency with good biocompatibility. To further evaluate the mucus-penetrating capabilities of the optimized peptides P25 TO P30, we tested their performance using an in vitro artificial mucus model. The results demonstrated that MNM exhibited the highest mucus penetration efficiency among all tested variants (fig. S15). These findings enabled us to establish key design principles for effective siRNA delivery to the lungs: N-terminal domains require moderate hydrophobicity to enable membrane penetration, central regions should include RNA-binding motifs such as His-rich sequences for effective siRNA compaction, and C termini must maintain a balanced hydrophilic sequence for mucus penetration.

To evaluate the cellular delivery efficiency of MN and MNM, we measured the fluorescence intensity of A549 cells following transfection with siRNA-Cy5. Both MN and MNM formulations resulted in approximately twofold higher fluorescence intensity compared to the Lipofectamine 2000 (Lipo2000) group (Fig. 1, F and G). In addition, we also performed a Western blotting experiment (fig. S16) to confirm the gene silencing efficacy of different cargos, showing that MNM–si*TGF-β1* NPs achieved significantly higher gene silencing efficiency than Lipo2000, which is consistent with their enhanced cellular uptake. Furthermore, neither MN-siRNA complexes nor MNM-siRNA NPs showed obvious cytotoxicity in HBE cells (fig. S17). On the basis of these results, we next explored the transfection rate toward various types of lung-resident cells. The delivery efficiency on bone marrow-derived macrophages (BMDMs) (Fig. 1H and fig. S18), bone marrow-derived dendritic cells (BMDCs) (fig. S19), and epithelial cells (Fig. 1I and fig. S20) was 92, 62, and 85%, respectively, indicating the high efficacy and versatility of MNM in cellular delivery.

To further validate the delivery system's functional efficacy, we evaluated gene knockdown efficiency in U2OS-RFP cells using three human-derived RFP-targeting siRNAs (table S8). hsiRFP-1 showed the highest silencing efficiency and was selected for subsequent screening (fig. S21). In the first-stage screening, several peptides demonstrated moderate gene silencing effects, whereas the MN showed the most efficient RFP knockdown (figs. S22 and S23). On the basis of this result, MN was selected as the lead carrier for further structural optimization. In the second-stage screening, the CLSM of U2OS-RFP cells and the mean fluorescence quantification showed that MNM exhibited the highest gene silencing efficiency among all tested peptides (figs. S24 and S25).

Characterization of peptide-siRNA NPs
Transmission electron microscopy (TEM) and dynamic light scattering (DLS) revealed that MN self-assembled into NPs with an average size of approximately 100 nm (fig. S26, A and B). Upon coassembly with siRNA, MN formed larger aggregates in a concentration-dependent manner, with increasing N/P ratios leading to greater particle size expansion (fig. S26C). Notably, at N/P = 20, the assemblies reached micrometer-scale dimensions, suggesting extensive aggregation under
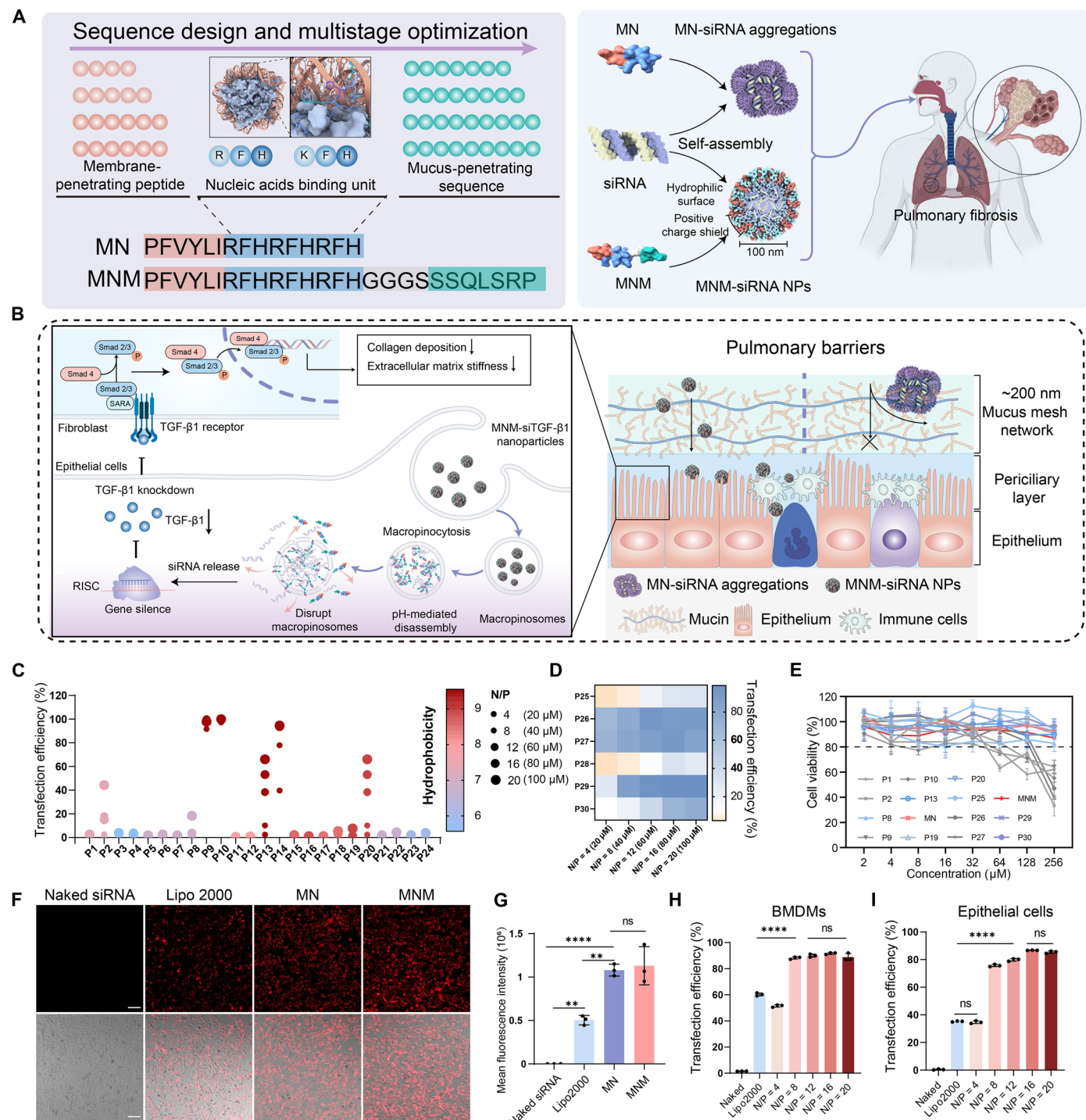
Fig. 1. Overview of the design and screening of peptide sequences for pulmonary siRNA delivery. (**A**) The design strategy and multistage screening of peptide sequences for pulmonary siRNA delivery. (**B**) The schematic illustration of barriers for pulmonary fibrosis gene therapy. (**C**) The siRNA delivery efficiency of peptides at various N/P ratios after treatment for 6 hours ($n = 3$). The color gradient reflects differences in peptide hydrophobicity. (**D**) The heatmap of siRNA delivery efficiency on A549 cells after treatment with peptide-siRNA NPs for 6 hours ($n = 3$). (**E**) The cytotoxicity of peptides on HBE cells after treatment for 24 hours ($n = 3$). (**F**) Representative CLSM images of A549 cells after transfection of siRNA-Cy5 using Lipo2000, MN (N/P = 12), and MNM (N/P = 12). Scale bars, 100 μm. (**G**) Quantification of fluorescence intensity of siRNA-Cy5 ($n = 3$). (**H** and **I**) The siRNA delivery efficiency in (H) BMDMs and (I) epithelial cells after treatment with MNM-siRNA NPs for 6 hours. siRNA is labeled with Cy5.

highly cationic conditions (fig. S26D). Such aggregation is likely driven by the strong electrostatic interactions between the positively charged C-terminal region of MN and the negatively charged siRNA, leading to interparticle cross-linking.

To prevent aggregation and enhance mucus penetration, we engineered MNM, a modified variant capable of forming stable NPs with an average size of approximately 80 nm upon assembly with siRNA, without detectable aggregations (Fig. 2, A and B). In addition, MNM also forms NPs with an average diameter of 80 nm (fig. S27). Furthermore, zeta potential measurements showed a gradual increase in surface charge with increasing N/P ratios for MN-siRNA complexes, reaching approximately +20 mV at N/P = 20 (fig. S26E), which is not conducive to mucus penetration, as particles with moderate positive or neutral charge show better mobility in mucus compared to highly charged particles (*17*). In comparison, the surface charge of MNM-siRNA NPs was approximately +10 mV at an N/P ratio of 20, suggesting that MPS modification effectively shields the cationic NP surface (Fig. 2C). This reduction in surface charge is beneficial for mucus penetration, as highly cationic particles are shown to exhibit poor mucus permeation due to strong electrostatic interactions with negatively charged mucin glycoproteins. In contrast, NPs with neutral or mildly cationic surfaces typically exhibit enhanced mobility through the mucus layer, making them more efficient for pulmonary delivery (*55*). Circular dichroism (CD) spectroscopy confirmed that the random coil structure of peptide MN and MNM remained unchanged after siRNA binding, suggesting that the peptide's secondary structure is not disrupted during complexation (Fig. 2D and fig. S26F). Multi-SIM microscopy confirmed efficient siRNA packaging and colocalization within the NPs (Fig. 2E), demonstrating the robustness of the MNM design (*56*).

Pulmonary siRNA delivery efficiency in vivo

To investigate the siRNA delivery efficiency of the peptide-based system in vivo, we performed fluorescence imaging of mice following intratracheal administration with peptide-siRNA assemblies (fig. S28). The siRNA-Cy5 in the MNM group was predominantly retained in the lung, with minimal distribution to other organs. In contrast, the fluorescence signal in the lung of Lipo2000 and MN groups was significantly lower, indicating reduced lung retention. Notably, naked siRNA is metabolized rapidly by the kidney and liver. Quantification of fluorescence intensity in major organs showed that MNM siRNA-Cy5 presented 2.07- and 1.93-fold higher mean fluorescence intensity than the Lipo2000 and MN group, respectively (Fig. 2, F and G). We further characterized the pulmonary retention kinetics of MNM-siRNA following intratracheal administration (Fig. 2H). MNM-siRNA demonstrated significantly prolonged lung residence ($t_{1/2} = 5.79$ hours) compared to PEI-siRNA ($t_{1/2} = 2.01$ hours), indicating the superior mucus-penetrating and lung-retention capabilities of the MNM NPs (Fig. 2I and fig. S29). Subsequently, we investigated the tissue distribution of MNM-siRNA NPs over time following intratracheal injection (Fig. 2J). The results demonstrated that MNM-siRNA NPs were primarily retained in the lung for up to 4 hours and were gradually degraded and cleared by the kidney (Fig. 2K). This time-dependent distribution profile highlights the prolonged lung retention and controlled clearance of MNM-siRNA NPs, suggesting that MNM-siRNA NPs require a lower dosage while also presenting a reduced risk of side effects.

To further evaluate the pulmonary siRNA delivery efficiency, we performed immunofluorescence staining on lung sections 6 hours

postintratracheal administration (Fig. 2L). Compared to naked siRNA, Lipo2000, and MN-siRNA complexes, which showed limited and sporadic siRNA delivery distribution in airway, the MNM group exhibited a widespread and intense fluorescence signal across both large and small airway epithelial cells, together with the distribution on alveoli surface. Such enhanced delivery to airway and the alveoli region demonstrated the superior coverage of our delivery system, underscoring the target effects to various diseased cells. This robust delivery efficiency of MNM-siRNA NPs was further quantified, revealing a significant improvement over Lipo2000 and MN carriers (Fig. 2M).

Mechanism of MNM-siRNA NPs overcoming the cellular barriers

A major challenge for intracellular gene delivery is achieving endosomal escape to release therapeutic cargo into the cytosol. To investigate how MNM-siRNA NPs overcome the cellular barrier, we used confocal laser scanning microscopy (CLSM) to track the endocytosis process. After incubating A549 cells with MNM-FITC (fluorescein isothiocyanate)/siRNA NPs for 0.5 hours, the cell membrane was stained with Deep Red plasma membrane dye. Images revealed distinct colocalization between the NPs and the cell membrane (fig. S30), indicating early-stage interactions of NPs with the cell membrane. To further investigate the cellular uptake dynamics, real-time internalization of MNM/siRNA-Cy5 NPs was monitored, and cells were stained with Lysotracker (Green). Confocal imaging revealed that the MNM-siRNA NPs exhibited minimal colocalization with lysosomes throughout the internalization process (fig. S31 and movies S1 to S3). By 2 hours, the NPs had entered the cells but showed no colocalization with lysosomes, indicating that MNM/siRNA-Cy5 NPs avoided lysosomal degradation (Fig. 3A). Similarly, MNM-FITC did not colocalize with lysosomes, further confirming the ability of MNM to evade lysosomal entrapment (fig. S32).

To reveal the internalization mechanism of MNM-siRNA NPs, we treated A549 with MNM-siRNA NPs in the presence of various endocytosis inhibitors and then quantified the siRNA delivery efficiency with flow cytometry (Fig. 3, B and C). The endocytosis inhibitor chlorpromazine (a clathrin-mediated endocytosis inhibitor) did not influence the endocytosis of MNM-siRNA NPs. Meanwhile, the siRNA delivery effect decreased from 90 to 45% in the presence of M-βCD, indicating that the internalization of MNM-siRNA NPs depended on the fluidity of the membrane. In addition, siRNA-Cy5 signals were observed in the cell cytoplasm at 4°C (Fig. 3D), indicating that some MNM-siRNA NPs penetrated the cell membrane directly without requiring active endocytic processes, while the cell membrane remained intact after this penetration (fig. S33). To further explore the involvement of energy-dependent uptake mechanisms, cells were treated with amiloride (a macropinocytosis inhibitor) and NaN$_3$ (an energy-dependent pathways inhibitor). Both treatments significantly reduced the uptake of MNM-siRNA NPs, indicating that macropinocytosis is the major endocytosis pathway of MNM-siRNA NPs (Fig. 3D and fig. S34). Furthermore, we investigated the endocytic mechanisms of MNM/siRNA NPs in MLE-12 cells (figs. S35 and S36) and primary epithelial cells isolated from fibrotic mouse lungs (figs. S37 and S38). The results indicated that macropinocytosis is the primary internalization route of MNM-siRNA NPs in pulmonary epithelial cells.

To further confirm macropinocytosis as the primary uptake pathway, we incubated cells with MNM-siRNA NPs and FITC-dextran, a
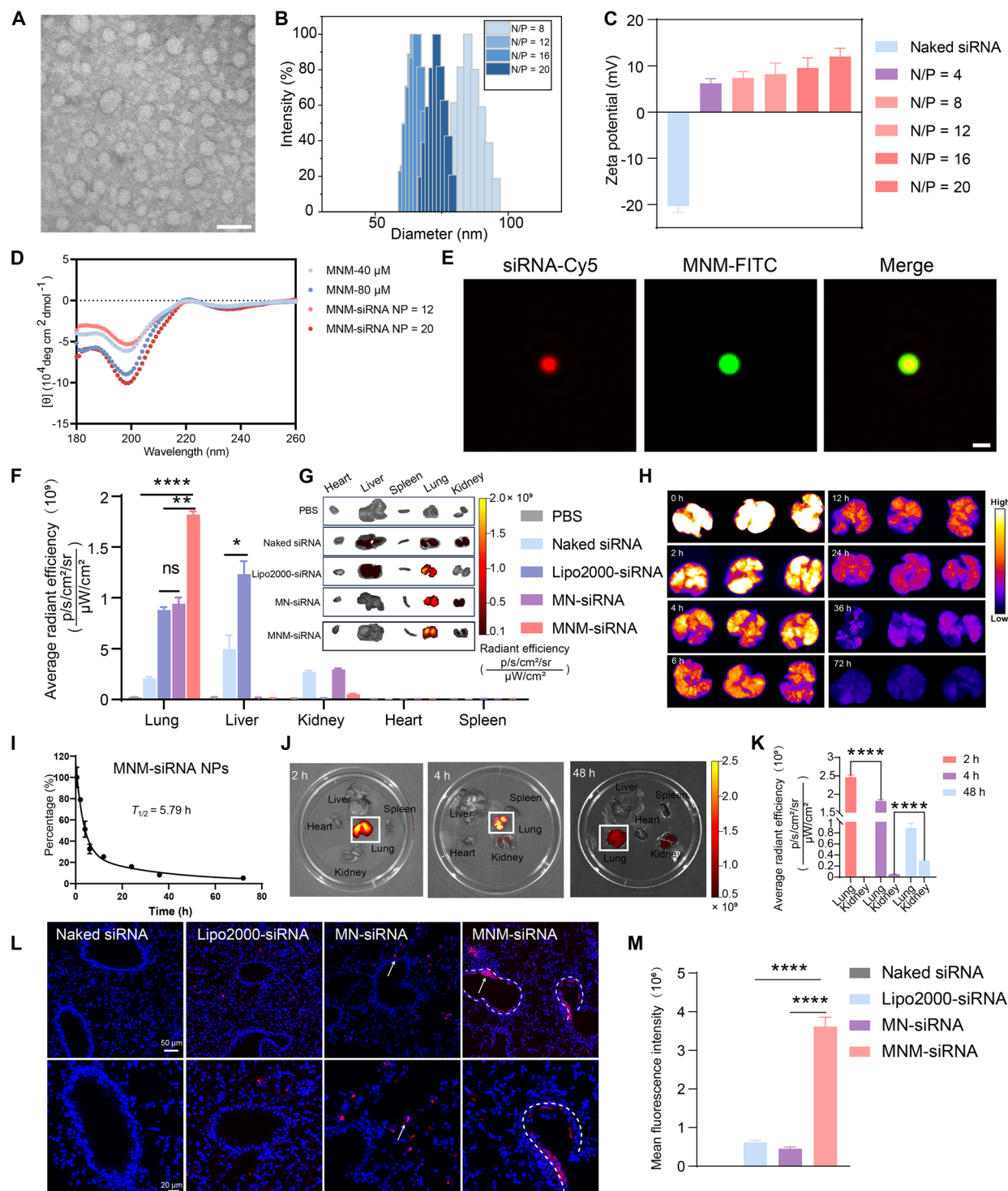
Fig. 2. Characterization of MNM-siRNA NPs and pulmonary delivery efficiency. (**A**) TEM image of MNM-siRNA NPs (N/P = 20). Scale bar, 200 nm. (**B**) DLS analysis of MNM-siRNA NPs at various N/P ratios. (**C**) Zeta potential of MNM-siRNA NPs at various N/P ratios. (**D**) CD spectra of MNM and MNM-siRNA NPs at various N/P ratios. (**E**) Multi-SIM microscopy images showing the colocalization of siRNA-Cy5 and MNM-FITC. Scale bar, 200 nm. (**F**) Quantitative analysis of fluorescence signals of mouse major organs. (**G**) Representative IVIS images of mouse major organs after intratracheal delivery of siRNA with Lipo2000, MN, and MNM. (**H**) Representative fluorescence images of mice lung after intratracheal administration of MNM/siRNA-Cy5 NPs (N/P = 20) at various time points. (**I**) Pulmonary retention kinetics of MNM-siRNA NPs following intratracheal administration. (**J**) Representative fluorescence images of major organs of mice after intratracheal administration of MNM-siRNA NPs (N/P = 20) at various time points. siRNA is labeled with Cy5. (**K**) Quantification of fluorescence signals in the lung and kidney at various time periods. (**L**) Representative immunofluorescence images of lung section after intratracheal delivery of siRNA-Cy5 with Lipo2000, MN, and MNM for 6 hours. The siRNA was labeled with Cy5 and nucleus were stained with DAPI. Scale bars, 50 μm (top) and 20 μm (bottom). (**M**) Quantification of fluorescence intensity in lung sections after delivery of siRNA-Cy5 with Lipo2000, MN, and MNM. (n = 3).
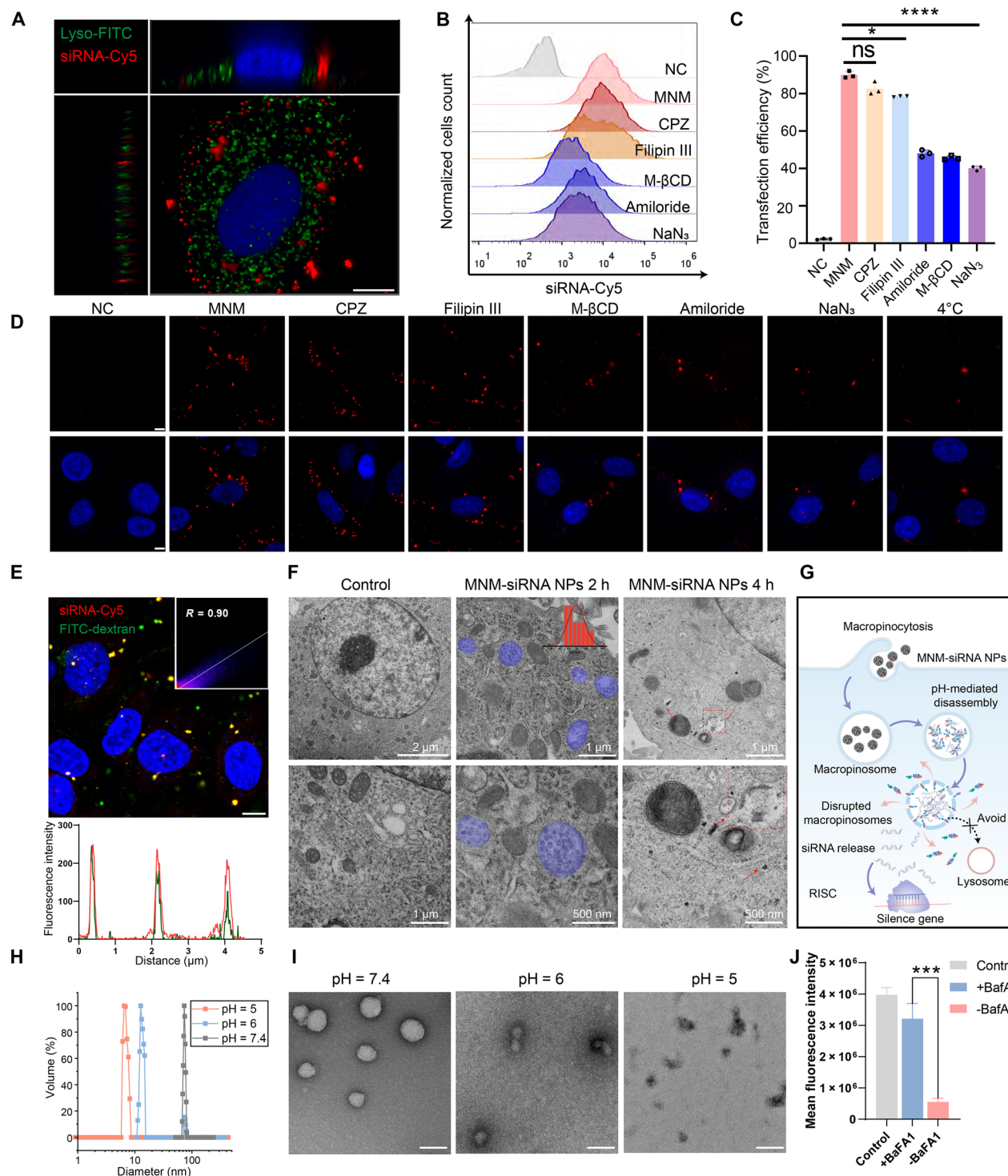
Fig. 3. Endocytosis mechanism of MNM-siRNA NPs. (**A**) CLSM images of A549 cells after treatment with MNM-siRNA NPs (N/P = 20) for 2 hours. The siRNA was labeled with Cy5, the cell nucleus was stained with Hoechst 33342, and lysosomes were stained with Lysotracker (green). Scale bar, 5 μm. (**B**) Endocytosis pathway analysis by flow cytometry. (**C**) Quantification of siRNA delivery efficiency in the presence of endocytosis inhibitors. (**D**) Representative CLSM images of A549 cells treated with various endocytosis inhibitors. Scale bars, 5 μm. (**E**) Colocalization of MNM/siRNA-Cy5 NPs with FITC-70 kDa dextran (macropinocytosis marker). Scale bar, 10 μm. (**F**) TEM images showing the endocytosis and release process of MNM-siRNA NPs. (**G**) Schematic illustration of macropinocytosis and endosome escape process of MNM-siRNA NPs. (**H**) The DLS characterizations of MNM-siRNA NPs at pH = 7.4, 6, and 5. (**I**) TEM images of MNM-siRNA NPs at pH = 7.4, 6, and 5. Scale bars, 100 nm. (**J**) RFP silencing efficiency by MNM-siRFP NPs in U2OS-RFP. U2OS-RFP cells were pretreated with or without 50 nM BafA1 for 1 hour to inhibit endosomal acidification before transfection.

well-established marker of macropinocytosis (*53*). CLSM images showed strong colocalization between MNM-siRNA NPs and FITC-dextran, providing additional evidence for macropinocytosis-mediated uptake (Fig. 3E). Furthermore, we used TEM to visualize the cellular uptake process of MNM-siRNA NPs. Clathrin-coated vesicles, which are typically ~100 nm in size, were not observed. Instead, MNM-siRNA NPs (~80 nm) were observed within larger vesicles (200 nm to 5 μm), consistent with macropinosomes (Fig. 3F) (*54*). MNM-siRNA NPs are internalized via the macropinocytosis pathway, after which the peptides appear to escape from macropinosomes before their fusion with lysosomes, enabling cytosolic delivery of siRNA (Fig. 3G). To investigate the mechanism of macropinosome escape, we examined the structural behavior of MNM-siRNA NPs under varying pH conditions. The TEM and DLS results revealed that MNM-siRNA NPs undergo pH-responsive disassembly in acidic environments (Fig. 3, H and I). This disassembly is triggered by protonation under acidic conditions, leading to the exposure of a hydrophobic, membrane-penetrating peptide segment that mediates membrane disruption (*57*). Furthermore, treatment of U2OS-RFP cells with bafilomycin A1 (BafA1), an inhibitor of the vacuolar-type H^+-ATPase proton pump, significantly reduces the gene silencing efficiency of MNM-siRNA NPs (Fig. 3J and fig. S39). Moreover, CLSM revealed that MNM-siRNA remained colocalized with FITC-dextran–labeled macropinosomes in BafA1-treated cells (fig. S40). Collectively, these data support the conclusion that macropinosomes' escape of MNM-siRNA NPs is dependent on macropinosomes' acidification and pH-responsive structural changes, which enable both NP disassembly and membrane disruption, thereby facilitating efficient siRNA delivery (*58*).

Penetration of pulmonary barrier and stability of MNM-siRNA NPs

To evaluate the importance of the MPS in overcoming the pulmonary mucus barrier, we first established an artificial mucus model (Fig. 4A). Naked siRNA was completely trapped in the mucus layer and failed to penetrate, while Lipo2000-siRNA NPs and MN-siRNA complexes showed limited penetration. In contrast, MNM-siRNA NPs exhibited significantly higher fluorescence intensity in the mucus layer at 0.5 hours, which further increased by 2 hours but stabilized thereafter (Fig. 4B). Furthermore, the DLS results showed that MNM-siRNA NPs at an N/P ratio of 20 maintained a stable size of 70 to 80 nm in healthy bronchoalveolar lavage fluid (BALF) for up to 4 hours (Fig. 4C). Subsequently, we cultured Calu-3 cells using transwell for 4 weeks to establish an air-interfaced culture (AIC) model (Fig. 4D), which mimics the airway epithelial barrier with secreted mucus layers (*59*). Comparative analysis revealed that MNM-siRNA NPs, modified with hydrophilic peptides, exhibited substantially enhanced mucus penetration versus unmodified MN-siRNA controls. This model confirmed that MNM-siRNA NPs could efficiently penetrate the mucus layer and reach the underlying epithelial cells (Fig. 4E).

To assess the stability of MNM-siRNA NPs in the lung microenvironment, we incubated the NPs in BALF from PF mice. In BALF from fibrotic lungs, the size of MNM-siRNA NPs increased from 100 to 200 nm, but no significant aggregation occurred, indicating their stability even in the harsh conditions of fibrotic lungs (fig. S41). Furthermore, we investigated the stability of MNM-siRNA NPs using TEM and DLS after 15 min of nebulization (fig. S42, A to C). The results indicated that the self-assembled MNM-siRNA NPs could

overcome the strong shear forces of nebulization, remaining stable without disruption or aggregation. The morphology of MNM-siRNA NPs postlyophilization and redissolution was an average size of approximately 100 nm, indicating that the MNM-siRNA NPs can be stored and transported in the dry powder form (fig. S42, D and E). In addition, the MNM-siRNA NPs still showed high delivery efficiency after lyophilization and redissolution (fig. S43)

Subcellular distribution of peptide-siRNA NPs in normal and fibrotic lungs of mice

We investigated the subcellular distribution of MNM-siRNA NPs in lung tissues using flow cytometry (Fig. 4F and fig. S44). In healthy mice, the siRNA delivery efficiency of MN-siRNA complexes and MNM-siRNA NPs was 7.37 and 18.32%, respectively, regarding total lung cells (Fig. 4G). Notably, MNM-siRNA NPs showed preferential targeting of lung epithelial cells, with 35.96% of Ep-CAM$^+$ epithelial cells, 16.88% of CD45$^+$ immune cells, and 9.80% of CD31$^+$endothelial cells exhibiting siRNA uptake (Fig. 4G). In contrast, MN-siRNA complexes primarily transfected endothelial cells (4.59% efficiency), with lower efficiency in epithelial (24.12%) and immune cells (7.71%). In addition, we performed immunofluorescence staining on lung sections. Epithelial cells were stained with Ep-CAM, and siRNA was labeled with Cy5. The immunofluorescence results demonstrated that siRNA-Cy5 was successfully delivered to airway epithelial cells in lung tissue (Fig. 4H).

Compared to healthy lungs, the pulmonary barrier in PF lungs is substantially harsher due to increased mucus viscoelasticity and thickening of the mucus layer (fig. S45A) (*60*). Histological analysis using hematoxylin and eosin (H&E) staining confirmed this difference, with normal lung tissue showing a thin, uniform mucus layer (fig. S45B), while PF lung tissue exhibited a thickened and irregular epithelial hyperplasia (fig. S45C). Immunofluorescence staining of fibrotic lung sections further confirmed that MNM-siRNA NPs effectively overcame the pulmonary barrier and localized predominantly in airway epithelial cells (fig. S45D). In fibrotic lungs, the delivery efficiency of MN-siRNA complexes and MNM-siRNA NPs decreased to 5.2% and 14.37%, respectively, reflecting the increased difficulty of penetrating the fibrotic mucus barrier (fig. S45E). However, MNM-siRNA NPs maintained their ability to target epithelial cells, with 26.79% of epithelial cells, 18.55% of immune cells, and 6.35% of endothelial cells showing siRNA uptake. (fig. S45F). In contrast, MN-siRNA complexes primarily transfected endothelial cells (3.74% efficiency), with lower efficiency in epithelial (13.97%) and immune cells (5.11%). These results highlight the superior targeting ability of MNM-siRNA NPs in both healthy and fibrotic lungs. This targeted delivery is critical for maximizing therapeutic efficacy while minimizing off-target effects, thereby enhancing the precision and safety of the intervention

Biocompatibility of peptide-siRNA NPs

To assess the biocompatibility of peptide-siRNA assemblies, we performed H&E staining on lung sections and major organs 24 hours after intratracheal administration (200 μg/kg). Histopathological analysis of major organs, including the heart, liver, and spleen, revealed no obvious toxicity. However, MN-siRNA complexes caused mild kidney injury, as evidenced by H&E staining (fig. S46). Furthermore, no signs of acute pulmonary inflammation or injury were observed in the lungs of mice treated with MNM-siRNA NPs (fig. S47A). We also evaluated systemic toxicity and inflammatory
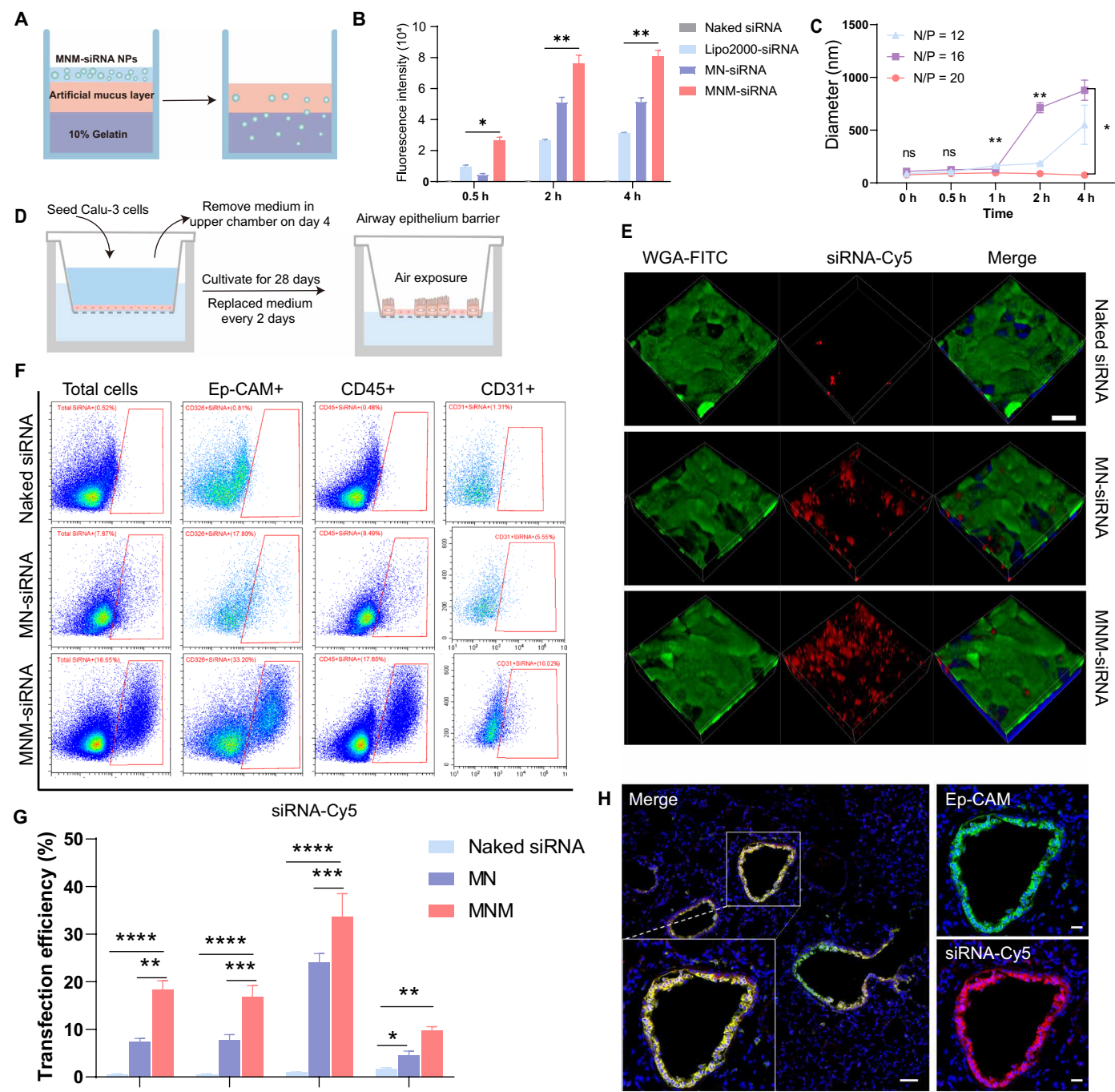
Fig. 4. Mucus penetration ability and biodistribution of peptide-siRNA assemblies. (**A**) Schematic illustration of the penetration of NPs in an artificial mucus model. (**B**) Quantitative analysis of fluorescence intensity of siRNA-Cy5 in the gelation layer. (**C**) Stability of MNM-siRNA NPs in BALF of healthy mice. (**D**) Scheme illustration of the air-interfaced culture (AIC) Calu-3 cell monolayer model construction. (**E**) Penetration of MNM-siRNA NPs into the AIC Calu-3 cell monolayers model and incubated for 6 hours. Scale bar, 20 μm. (**F**) Flow cytometry analysis of subcellular distribution of peptide-siRNA assemblies in the healthy lungs. (**G**) Quantification analysis of subcellular distribution of peptide-siRNA assemblies; siRNA was labeled with Cy5 (n = 3). (**H**) Immunofluorescence staining of normal lung section after delivery of siRNA with MNM for 6 hours. Scale bars, 20 μm.

responses by analyzing blood parameters after intratracheal administration of phosphate-buffered saline (PBS), naked siRNA, Lipo2000-siRNA NPs, MN-siRNA complexes, and MNM-siRNA NPs (200 μg/kg) for 24 hours. There was no significant abnormality in blood parameters, including red blood cell (RBC), hemoglobin (HGB), mean corpuscular volume (MCV), and mean corpuscular hemoglobin

(MCH), indicating that MNM-siRNA NPs did not induce hemolysis (fig. S47, B to E).

To comprehensively assess the long-term safety profile of MNM-siRNA NPs, we performed a 28-day repeated-dose toxicity study following respiratory tract exposure (fig. S48A). Hematological analysis demonstrated no clinically significant alterations in RBC count, HGB

concentration, MCV, and MCH between MNM-siRNA-treated mice and healthy controls (fig. S48, B to E), indicating the absence of hematopoietic toxicity following prolonged pulmonary administration.

Furthermore, we assessed lung function in mice treated with PBS, naked siRNA, Lipo2000-siRNA, or MNM-siRNA NPs, respectively. Pulmonary function assessment revealed comparable levels of inspiratory capacity (IC), forced expiratory volume in 0.2 s (FEV0.2), resistance of the respiratory system (Rrs), static compliance (Cst), forced vital capacity (FVC), and elastance (Ers) in the MNM-siRNA group and the healthy control group (fig. S48, F to K). Further histological examination of major organs—including the lungs, liver, spleen, kidney, and heart—at 4 weeks post–local administration of MNM-siRNA NPs revealed no signs of acute tissue injury (fig. S49). These findings suggest that MNM-siRNA administration shows excellent biocompatibility post–long-term treatment.

Therapeutic efficacy of MNM–si*TGF-β1* NPs in PF mice

To establish a model of PF, we administered bleomycin intratracheally to C57BL/6J mice at doses of 1.5 U/kg. Quantitative polymerase chain reaction (qPCR) data further showed a significant up-regulation of *TGF-β1* expression in comparison to healthy lungs, along with increased expression of other PF-related genes, including *COL1A-1*, *FN-1*, and *TN-C* (fig. S50). Subsequently, the histological analysis of lung sections confirmed the up-regulation of *TGF-β1* in fibrotic lungs of PF mice (fig. S51). *TGF-β1* is a profibrotic cytokine that plays a central role in epithelial-mesenchymal transition, fibroblast migration, and proliferation, thereby driving key pathological processes in PF (*61*). During the progression of PF, injured epithelial cells release increased levels of *TGF-β1*, which promotes collagen secretion, ECM accumulation, mediated through the canonical Smad signaling pathway (*62*). Therefore, targeting *TGF-β1* signaling represents a promising therapeutic strategy for fibrotic lung diseases (*63*, *64*).

Before in vivo studies, we first screened mouse-specific siRNA sequences targeting *TGF-β1* in primary epithelial cells isolated from fibrotic mouse lungs. Both qPCR and Western blotting analyses identified that msi*TGF-β1*-2 exhibited the highest silencing efficiency (fig. S52, A and B). Subsequently, Western blotting analysis confirmed that MNM–si*TGF-β1* NPs induced significantly higher *TGF-β1* silencing efficiency compared to Lipo2000 (fig. S52C).

Mice were treated with peptide–si*TGF-β1* NPs every 2 days following the establishment of the PF mice model (Fig. 5A). MNM–si*TGF-β1* NPs significantly improved survival rates compared to untreated controls (Fig. 5B). On day 21, histopathological analysis revealed that MNM–si*TGF-β1* NPs markedly attenuated the progression of fibrosis, evidenced by H&E staining showing reduced alveolar wall thickening (Fig. 5C). Masson's trichrome staining confirmed decreased collagen deposition in interstitial regions (Fig. 5, C and D), consistent with the H&E results (*15*).

High-resolution computed tomography (CT) imaging further validated these findings. 2D-CT scan demonstrated that MNM-siRNA NPs prevented the progression of PF, and three-dimensional (3D)–reconstructed images showed a significant decrease in fibrotic lesion volume (Fig. 5E). Periodic acid–Schiff (PAS) staining revealed fewer carbohydrate-rich structures (e.g., glycoproteins) in the MNM group, indicating reduced mucus hypersecretion compared to PBS and MN–si*TGF-β1* treated groups (Fig. 5F). qPCR analysis demonstrated that MNM–si*TGF-β1* NPs down-regulated *TGF-β1* expression in fibrotic lungs by 9.7-fold compared with the naked group. Fibrosis-related genes in the MNM group, including *COL1A-1* and

FN-1, were reduced by 1.5- and 7.1-fold, respectively, compared to the MN group (Fig. 5G). In addition, Western blotting analysis demonstrated that MNM–si*TGF-β1* significantly reduced TGF-β1 expression and decreased Smad2/3 phosphorylation (pSmad2/3), suggesting effective inhibition of the TGF-β1/Smad signaling pathway (fig. S53).

Encouragingly, MNM–si*TGF-β1* NPs restored normal respiratory function, as manifested by further pulmonary function tests (PFTs). MNM–si*TGF-β1* NPs mitigated the decline in IC, Cst, and respiratory system compliance (Crs) (Fig. 5, H to J). In addition, they reduced Rrs and Ers (Fig. 5, K and L) while improving FVC, a key clinical marker of fibrosis severity (Fig. 5M). Cytokine analysis in BALF showed reduced levels of proinflammatory cytokine interleukin-6 (IL-6) in the MNM group, further confirming therapeutic efficacy (Fig. 5N).

Fast processive PF therapy

PF is an irreversible and progressive disease, with increasing risks of severe complications and mortality as the pathology advances. The progression of PF is difficult to predict, as it depends on underlying factors and other risks (*65*). To evaluate the therapeutic potential of MNM–si*TGF-β1* NPs in halting aggressive disease progression, we established a fast-progressive PF model by intratracheal administration of bleomycin (3 U/kg) to C57BL/6J mice, then mice were treated with peptide–si*TGF-β1* assemblies every 2 days for 2 weeks (Fig. 6A). The micro-CT monitoring of lung fibrosis progression revealed that the 3-U/kg dose induced more severe fibrotic lesion volume (fig. S54). In this aggressive model, mice treated with naked siRNA experienced respiratory failure and died within 8 days. In contrast, treatment with MN–si*TGF-β1* complexes improved survival rates to 30%, while MNM–si*TGF-β1* NPs further increased survival to 50% (Fig. 6B).

Further histological analysis revealed that MNM–si*TGF-β1* NPs substantially reduced airway thickness and alveolar fusion (Fig. 6C and fig. S55). In addition, inflammatory cell infiltration was markedly decreased in the MNM group, indicating reduced disease severity. Masson's trichrome staining further confirmed that fibrotic deposition and collagen accumulation in both airway and alveolar regions reduced after treatment with MNM–si*TGF-β1* NPs (Fig. 6D). Quantitatively, MNM–si*TGF-β1* NPs reduced collagen deposition by 21.4% in airway sections and 23.4% in alveolar sections compared to the MN group (Fig. 6, E and F).

qPCR analysis demonstrated that MNM–si*TGF-β1* NPs significantly down-regulated the expression of fibrosis-related genes, including *COL1A-1*, *FN*, *TN-C*, and α-*SMA* by 7.64-, 3.65-, 4.32-, and 5.03-fold reductions, respectively, compared to the naked group (Fig. 6G). To investigate the impact on the profibrotic immune microenvironment, we analyzed cytokines in BALF. Overexpression of IL-13 and MCP-1 (CCL2) in PF drives M2 macrophage polarization via the MCP-1/CCR2 axis, promoting type 2 immune responses and fibrosis progression. Treatment with MNM–si*TGF-β1* NPs significantly reduced the levels of IL-13 (Fig. 6H) and MCP-1 (Fig. 6I) compared to the bleomycin control group. In addition, the proinflammatory cytokine IL-6 was down-regulated in the MNM group by 3.92-fold (Fig. 6J).

Immunofluorescence assays further validated these findings; the numbers of CD68^{+}CD163^{+} profibrotic M2 macrophages were significantly up-regulated in fibrotic lungs compared to healthy controls. However, treatment with MNM–si*TGF-β1* NPs markedly reduced M2 macrophage infiltration (fig. S56). Furthermore, immunofluorescence
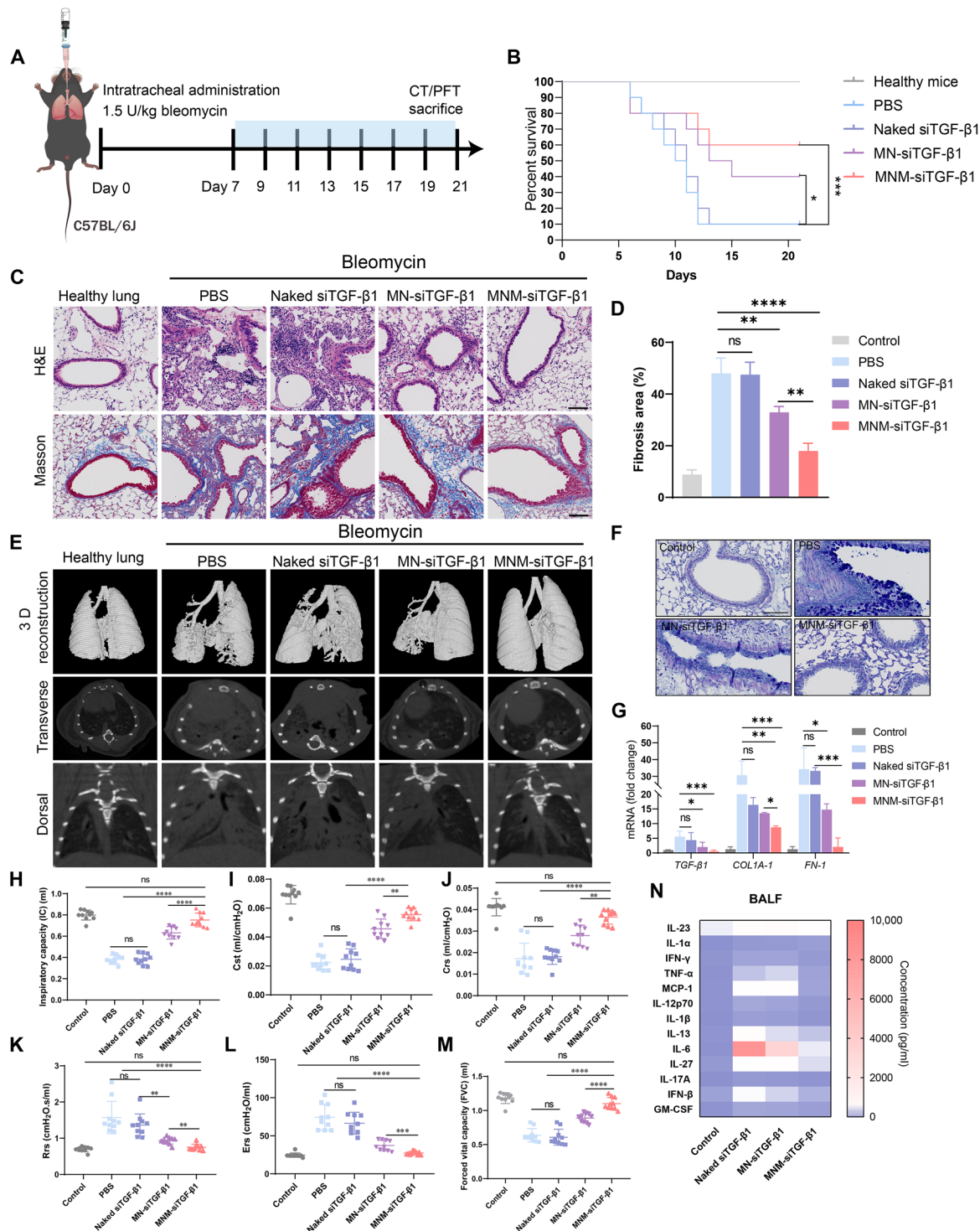
Fig. 5. Therapeutic effects of peptide–si*TGF*-β*1* assemblies. (**A**) Schedule for bleomycin-induced PF model building and treatment with peptide–si*TGF*-β*1* assemblies. Ten-week-old C57BL/6J mice were induced with bleomycin (1.5 U/kg) for 1 week to establish the pulmonary fibrosis model. The mice were treated with peptide–si*TGF*-β*1* assemblies for 2 weeks (*n* = 10). (**B**) Survival assessment of PF mice after treatment with peptide–si*TGF*-β*1* assemblies (*n* = 10). (**C**) H&E and Masson staining of mouse lung sections after treatment with peptide–si*TGF*-β*1* assemblies for 2 weeks. Scale bars, 200 μm. (**D**) Quantification of Masson staining of lung sections. (**E**) Representative micro-CT images of lungs after treatment with peptide-siRNA assemblies for 2 weeks. (**F**) PAS staining of the lung section after treatment with peptide–si*TGF*-β*1* assemblies. Scale bar, 300 μm. (**G**) qPCR analysis of expression of PF related gene in PF lungs (*n* = 3). (**H** to **M**) The pulmonary function tests (PFTs) of PF mice after treatment with peptide–si*TGF*-β*1* assemblies (*n* = 10). (**N**) Heatmap of inflammation cytokine levels in BALF.
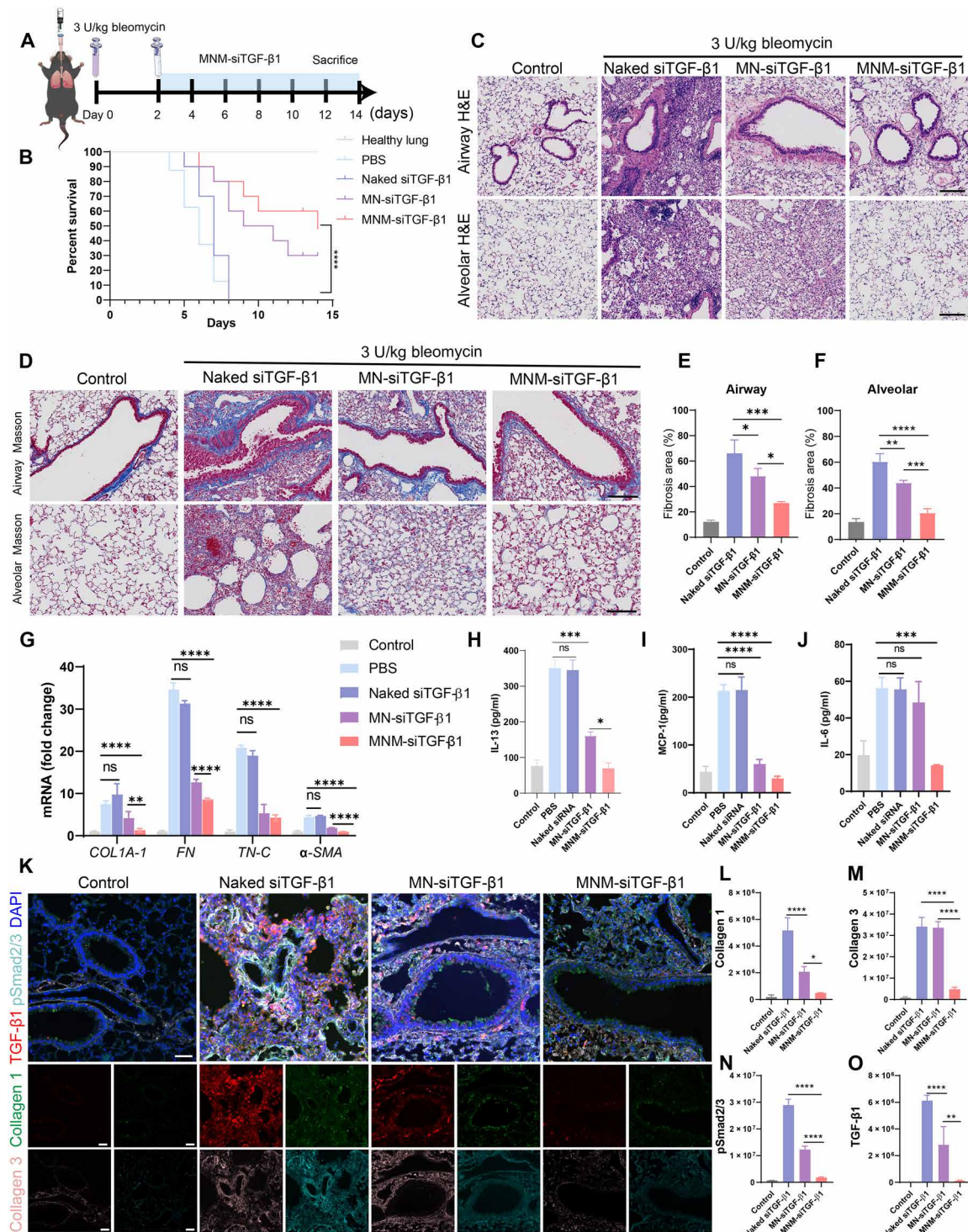
Fig. 6. Pulmonary fibrosis therapy with peptide–si*TGF-β1* assemblies in serious bleomycin-induced PF model. (**A**) Schedule for bleomycin injection and treatment with peptide–si*TGF-β1* assemblies. (**B**) Survival assessment of PF mice (*n* = 10). (**C**) H&E staining of the airway section and alveolar section. Scale bars, 300 μm. (**D**) Masson staining of the lung section after treatment with peptide–si*TGF-β1* assemblies. Scale bars, 100 μm. (**E** and **F**) Quantification of Masson staining of the airway section and alveolar section. (**G**) qPCR analysis of expression of the PF-related gene in PF lungs after treatment with peptide–si*TGF-β1* assemblies (*n* = 3). (**H** to **J**) Analysis of inflammatory cytokines in the serum of PF mice after treatment with peptide–si*TGF-β1* assemblies. (**K**) Immunofluorescence staining of Collagen 1 (green), Collagen 3 (pink), pSmad2/3 (cyan), and TGF-β1 (red). The nucleus was stained with DAPI (blue). Scale bars, 50 μm. (**L** to **O**) Quantification of Collagen 1, Collagen 3, pSmad 2/3, and TGF-β1 in the lung section.

staining suggested that MNM–si*TGF-β1* NPs down-regulated the expression of key profibrotic mediators, including TGF-β1, pSmad2/3, Collagen 1, and Collagen 3 (Fig. 6K). Quantification of immunofluorescence results revealed that MNM–si*TGF-β1* NPs achieved a significant reduction in these markers compared to the naked siRNA group, highlighting their potent antifibrotic effects (Fig. 6, L to O).

DISCUSSION

PF presents formidable challenges for gene therapy due to the complex and harsh pulmonary barriers, including the mucus layer, cellular membranes, and lysosomal degradation (*24*, *55*). In this work, we established a modular peptide platform for pulmonary siRNA delivery, addressing critical barriers in PF therapy with several key properties: (i) high-efficiency nucleic acid packaging, (ii) cellular membrane penetration and endosome escape, (iii) mucus layer penetration, (iv) stability postnebulization, and (v) excellent biocompatibility (*25*, *26*). During the construction of optimal delivery vehicle MNM, the precise design of a nucleic acid–binding peptide sequence (RFHRFHRFH) secures the stable packaging of siRNA. The further incorporation of a hydrophobic membrane–penetrating peptide facilitates cellular uptake and endosomal escape, while a mucus-penetrating peptide overcomes the dense mucus barrier (*52*). By combining these three functional modules, we engineered a highly efficient pulmonary siRNA delivery platform, termed MNM.

In summary, MNM-siRNA NPs demonstrate superior mucus-penetrating capabilities and show promising efficacy in siRNA delivery and the treatment of PF. Their resistance to shear stress during nebulization and excellent biocompatibility further highlight their great potential for clinical application. Furthermore, MNM-siRNA NPs retain full biological activity after freeze-drying and reconstitution, enabling long-term storage and transport in powder form. As a peptide-based carrier, MNM can be efficiently synthesized via solid-phase peptide synthesis, offering advantages in scalability, reproducibility, and quality control over complex systems such as exosomes or polymers. While the current formulation is simple and reproducible, further optimization and rigorous quality control need further investigation.

In addition, we also explored the delivery efficiency of our system MNM for long nucleic acid sequences including mRNA, plasmid, and circular RNA (circRNA). MNM achieved a delivery efficiency of approximately 60, 90, and 95% for plasmid-RFP, mRNA-mCherry, and circRNA mCherry in human embryonic kidney 293T cells, respectively (figs. S57 to S59). However, the mRNA delivery efficiency of MNM was around 40% in hard-to-transfect BMDCs (figs. S60 and S61). These findings also underscore the therapeutic potential of the MNM gene delivery system as a versatile platform for the delivery of diverse types of nucleic acids, opening new avenues of peptide-based gene delivery systems. However, certain limitations of the current formulation must be acknowledged. The current formulation lacks cell-specific targeting, which restricts its ability to selectively deliver nucleic acids to specific cell types. Future studies will focus on functional modifications of the MNM platform to enhance cell-specific delivery.

MATERIALS AND METHODS
Study design

The objective of this study was to develop an inhalable peptide-based gene delivery system for PF therapy, designed to overcome pulmonary barriers and achieve highly efficient delivery to pulmonary epithelial cells. To develop the MNM pulmonary siRNA delivery system, we conducted multistage screening and optimization of peptide sequences by evaluating siRNA delivery to A549 cells using flow cytometry. In vitro experiments were conducted with three or more replicates, including MNM system characterization, siRNA transfection efficiency quantification, and other assessments. Pulmonary siRNA delivery efficiency in vivo was evaluated using IVIS and IF staining. The sample size for in vivo experiments was determined based on previous related studies. Outlier evaluation was not conducted, and no data were excluded from the analysis. We established a PF mouse model using bleomycin to assess the treatment efficacy of MNM–si*TGF-β1* NPs. Mice were randomly assigned to different treatment groups, with a maximum of 10 animals per group according to the license protocol. During the therapy process, we stopped data collection and euthanized the mice when the mice became moribund and the body weight loss was greater than 15%.

Statistical analysis

Analysis of all data was conducted using Student's t test or analysis of variance (ANOVA) with Tukey's post hoc test, followed by multiple comparisons using GraphPad Prism software (version 9.5, GraphPad Software). The statistical significance of differences in survival analysis was evaluated using the log-rank (Mantel-Cox) test. Significant differences are indicated as follows: ns (not significant), $P \geq 0.05$, $*P < 0.05$, $**P < 0.01$, $***P < 0.001$, and $****P < 0.0001$.

Animals

C57BL/6J mice (male, 6 to 10 weeks old) were purchased from Vital River Laboratory Animal Technology Co., Ltd. (Shanghai, China) and housed under specific pathogen–free conditions: environment temperature, $24 \pm 2°C$; air humidity, 40 to 70%; and 12-hour dark/12-hour light cycle. All animal studies were approved by the Institutional Animal Care and Use Committee (IACUC) of Westlake University (IACUC protocol no. 21-046-WHM and no. 25-029-WHM).

Formulation of peptide-siRNA NPs

Peptide-siRNA NPs were prepared through the self-assembly of peptide and siRNA molecules. We diluted nucleic acids and peptides to the final concentrations at different N/P ratios (the ratio between nitrogen residues in peptide and nucleic acid phosphate groups) (4, 8, 12, 16, 20) with RNase-free water. The diluted peptides were then dropped into the siRNA solution at a 1:1 volume ratio, and the mixture was incubated for 45 min to allow for self-assembly into NPs.

TEM measurements

The morphologies of peptide self-assemblies and peptide-siRNA nanocomplexes were characterized with a 120-kV transmission electron microscope (Thermo Fisher Scientific, USA). First, a 5-μl sample was loaded on the carbon-coated grid, and the extra solution was removed with a piece of filter paper. The sample was stained with 2% uranyl acetate for 1 min. After removing the extra uranyl acetate and drying in vacuum, we used TEM to observe the sample directly.

DLS measurements

The zeta potential and hydrodynamic size of peptide-siRNA nanocomplexes in H_2O (pH 7.4) were measured by DLS (BI-200SM NanoBrook ZetaPALS) at 25°C. The peptide-siRNA nanocomplexes were prepared at N/P ratios of 4, 8, 12,16, and 20, using a constant

1 µg of siRNA for particle preparation. Each sample was analyzed for 90 s and repeated three times.

CD spectrum

We measured the CD spectrum of peptide and peptide-siRNA nanocomplexes with the Chirascan V100 Circular Dichroism Spectrometer. The peptides were diluted with ddH$_2$O and incubated for 45 min. Equi volume aqueous solutions of peptide and scrambled siRNA (100 µl each) were mixed at N/P ratios of 4, 8, 12, 16, and 20.

Analyzing siRNA transfection efficiency by flow cytometry

To screen the peptide delivery carriers and analyze their transfection efficiency, A549 cells were seeded in 24-well plates at a density of 1×10^5 cells per well and incubated overnight. The FAM-labeled Lipo-siRNA or peptide-siRNA complexes were added at various N/P ratios (N/P = 4, 8, 12, 16, and 20) and incubated for 6 hours. Subsequently, we collected the cells and washed them three times with PBS. Dead cells were stained with LIVE/DEAD Fixable Blue Dead Cell Stain Kit (Thermo Fisher Scientific). The transfection efficiency was then assessed using flow cytometry.

Analyzing siRNA transfection by CLSM

A549 cells were seeded in 24-well plates at a density of 1×10^5 cells per well and incubated overnight. The FAM-labeled Lipo-siRNA or peptide-siRNA complexes were added at various N/P ratios (N/P = 4, 8, 12, 16, and 20) and incubated for 6 hours. Subsequently, we analyzed the cells using CLSM.

Cell viability assay

We test the cytotoxicity of peptide with MTT assay. Briefly, 2×10^4 HBE cells per well were seeded in 96-well plates and cultured for 12 hours. The peptides at different concentrations were added into the culture medium and incubated for 24 hours. Ten microliters of MTT (5 mg/ml) was added into each well and incubated for 4 hours. Then, 100 µl of sodium dodecylsulfate-HCl solution was added to each well and incubated overnight. Last, the absorbance was measured at 490 nm using the Microplate Reader (Varioskan Lux, Thermo Fisher Scientific, USA).

siRNA delivery efficiency in vivo

The mice were intratracheally administrated naked siRNA, Lipo2000-siRNA, MN-siRNA complexes, and MNM-siRNA NPs ($n = 3$). Mice were euthanized at 6 hours posttreatment, and lungs were collected. The lungs were fixed in 4% paraformaldehyde and embedded in optimal cutting temperature compound. Lungs were sectioned at 10-µm intervals on a Cryostat (Thermo Fisher Scientific, USA) and stained with 4′,6-diamidino-2-phenylindole (DAPI). The samples were observed with CLSM, and fluorescence images of the pulmonary section were acquired. For each mouse, three different fields of the sections from the same position of the lungs were imaged and analyzed. ImageJ software was used to quantify the percentage of area with a positive fluorescence signal from peptide/siRNA-Cy5 NPs in lung tissue sections.

Biodistribution of peptide-siRNA NPs

The mice were intratracheally administrated Cy5-labeled naked siRNA, Lipo2000-siRNA, MN-siRNA complexes, and MNM-siRNA NPs (N/P = 20) at a dose of 200 µg/kg. The biodistribution was monitored using a PE Spectrum small animal imaging system. Subsequently, the mice were euthanized, and organs were harvested and imaged.

Distribution of NPs in the PF lungs analyzed by flow cytometry

Ten-week-old C57BL/6J mice ($n = 3$) were intratracheally administered MNM-siRNA NPs at a dose of 200 µg/kg. Mice were euthanized 6 hours posttreatment, and lungs were collected. The lungs were minced and digested in PBS containing collagenase I, 0.92 M Hepes, and DNase I at 37°C for 1 hour. The samples were subsequently incubated with antibodies to identify epithelial cells (EpCAM$^+$), immune cells (CD45$^+$), and endothelial cells (CD31$^+$). Then, the samples were analyzed with flow cytometry to determine the distribution of the NPs among these cell types.

Cellular uptake of MNM-siRNA NPs

To investigate the intracellular distribution of MNM-siRNA NPs, A549 cells were seeded in a confocal dish at a density of 1×10^5 cells/ml and incubated overnight. The MNM-siRNA NPs were added and incubated for 2 hours. Subsequently, cells were stained with Hoechst (Blue) and Lyso-Tracker (Red). The cells were then observed under a 63× oil objective on a Leica confocal microscope.

Endocytosis mechanism of peptide MNM-siRNA NPs

To investigate the endocytosis mechanism of MNM/siRNA-Cy5 NPs in A549 cells, we used major endocytosis inhibitors to coincubate with the cells and assessed cellular uptake using flow cytometry and CLSM. We preincubated the cells with the inhibitors for 30 min, followed by the addition of the MNM-siRNA NPs and a subsequent coincubation period of 2 hours. The concentrations of the inhibitors were 5 mM for M-βCD, 1 mM for amiloride, 40 µM for chlorpromazine, 100 mM for sodium azide (NaN$_3$), and 1.5 µM for filipin III. At the designated time points, we collected the cells, centrifuged them, and resuspended the pellets. Cellular uptake was then determined using flow cytometry and CLSM.

Primary epithelial cells isolated from fibrotic mouse lungs

Eight-week-old C57BL/6J mice were intratracheally instilled with bleomycin sulfate at a dose of 3 U/kg to induce PF. One week post–bleomycin induction, lungs were harvested and perfused via the right ventricle with PBS to remove residual blood. The lung tissues were then minced into small fragments and digested in PBS supplemented with collagenase I (1 mg/ml), Hepes (0.92 M), and DNase I (10 µg/ml) for 1 hour at 37°C with gentle agitation. Following digestion, the tissue suspension was sequentially filtered through a 70-µm cell strainer to obtain a single-cell suspension. RBCs were lysed using lysis buffer, and the remaining cells were washed and resuspended in PBS containing 2% fetal bovine serum. For epithelial cell isolation, cells were incubated with fluorescently labeled antibodies against EpCAM (Alexa Fluor 647, a marker for epithelial cells) and subsequently sorted by fluorescence-activated cell sorting.

Western blotting analysis of si*TGF*-β1 silencing efficiency in A549 cells

Three siRNA sequences were designed for targeting human-derived *TGF*-β1 mRNA, synthesized by Sangon Biotech. The sequences of hsi*TGF*-β1 are summarized in table S4. A549 cells were seeded in 12-well plates at a density of 2×10^5 cells per well and incubated for 12 hours. The cells were transfected hsi*TGF*-β1-1/2/3 (1 µg per well) with Lipo2000 for 24 hours. Western blotting (WB) was used to analyze *TGF*-β1 silencing efficiency. Subsequently, cells were treated with naked hsi*TGF*-β1, Lipo2000-hsi*TGF*-β1, MN-hsi*TGF*-β1, and

MNM-h*siTGF-β1* for 48 hours (0.5 μg per well). The cells were lysed by radioimmunoprecipitation assay (RIPA) lysis buffer (catalog no. P0013B, Beyotime) and then centrifuged (12,000 rpm, 10 min) to collect the supernatant. The concentration of protein solution was detected using a bicinchoninic acid (BCA) protein assay kit (catalog no. P0012S, Beyotime). The sample were separated on 12% SDS–polyacrylamide gel electrophoresis and transferred to a polyvinylidene difluoride (PVDF) membrane. Subsequently, the membranes were blocked with 5% milk and then incubated overnight at 4°C with primary antibodies: β-tubulin Rabbit mAb (A12289, 1:1000 dilution) and TGF-β1 Rabbit mAb (ab215715, 1:5000 dilution). Following this, the PVDF membranes were incubated with their corresponding secondary horseradish peroxidase (HRP)–conjugated antibodies (1:3000 dilution).

Building of artificial mucus model
Briefly, artificial mucus was prepared by adding 50 mg of DNA, 25 mg of mucin, 25 mg of sterile egg yolk emulsion, 29.5 μg of diethylenetriamine pentaacetic acid, 25 mg of NaCl, 11 mg of KCl, and 0.1 ml of RPMI 1640 to 5 ml of water. The mixture was stirred overnight to obtain a homogeneous dispersion. A 10% (w/v) gelatin solution (1 ml) was added to a 24-well plate and hardened at room temperature. Subsequently, the surface of the gelatin layer was covered with the artificial mucus, followed by the addition of siRNA delivery cargos. The samples were incubated for designated periods of time. Last, the artificial mucus was removed, and the fluorescence intensity of the gelatin was measured to determine whether the siRNA-Cy5 delivery cargos had penetrated the mucus layer.

In vitro penetration assay using AIC of the Calu-3 cell model
The AIC of the Calu-3 cell model could secrete mucus layers, serving as a well-established in vitro model to assess the penetration ability of NPs. Calu-3 cells were seeded into the apical chamber of the Transwell inserts at a density of 2×10^5 cells per well with 150 μl of culture medium. Medium (800 μl) was added to the basal chamber. The plate was placed in a humidified 37°C/5% CO_2 incubator overnight. To form the air-liquid interface, the culture medium in the apical chamber was removed after seeding for 4 days. The cells were subsequently cultured with 500 μl of culture medium in the basal chamber for 28 days, with the medium being changed every 2 days. Peptide/siRNA-Cy5 assemblies (N/P = 20, 1 μg of siRNA-Cy5) were then added to the apical side in 200 μl. After incubation at 37°C for 6 hours, the cell monolayers were washed three times with PBS. Mucin was stained with FITC-conjugated wheat germ agglutinin (5 μg/ml) for 15 min, followed by two PBS washes. Nuclei were then stained with Hoechst (Blue), and a 3D analysis of Z-stack images was conducted from the apical to basal side of the monolayer using CLSM.

The stability of MNM-siRNA NPs
To evaluate the stability of MNM-siRNA NPs in BALF, we incubated MNM-siRNA NPs with BALF from both healthy mice and mice with PF for 0.5, 1, 2, and 4 hours. Subsequently, DLS was used to test the size changes. Furthermore, we evaluated the stability of MNM-siRNA NPs after nebulization for 15 min with TEM and DLS.

PF mice model and its therapy with peptide–si*TGF*-β1 assemblies
Wild-type C57BL/6J mice (male, 10 to 12 weeks) received a single intratracheal instillation of bleomycin sulfate (MeilunBio, MA0186) at doses of 1.5 and 3 U/kg, dissolved in 50 μl of sterile saline. The mice in the control group received an equal volume of PBS via intratracheal injection. Subsequently, the PF mice were intratracheally administrated with naked siRNA, MN–si*TGF*-β1, and MNM–si*TGF*-β1 NPs every 2 days. Body weight was recorded daily, and micro-CT and PFTs were performed after 2 weeks of therapy.

WB and qPCR analyzing down-regulation of *TGF*-β1 in vitro and in vivo
To knock down *TGF*-β1 in PF mice, a series of siRNA sequences targeting murine *TGF*-β1 mRNA were synthesized by Sangon Biotech, as listed in table S5. The msi*TGF*-β1 sequences were transfected into mouse primary epithelial cells using Lipofectamine 2000 for 24 hours. Total RNA was extracted using TRIzol, and *TGF*-β1 mRNA expression levels were quantified by qRT-PCR. The silencing efficiency of *TGF*-β1 in mouse primary epithelial cells was further evaluated by Western blotting analysis, as previously described.

After bleomycin (1.5 U/kg)–induced PF mice were treated with peptide–si*TGF*-β1 NPs for 2 weeks, lung tissues were collected and homogenized in RIPA lysis buffer. The homogenates were centrifuged at 12,000 rpm for 10 min to obtain protein extracts. Protein concentrations were determined using a BCA protein assay kit (catalog no. P0012S, Beyotime). The protein samples were separated by 12% SDS–polyacrylamide gel electrophoresis and transferred onto PVDF membranes. Membranes were then blocked with 5% nonfat milk and incubated overnight at 4°C with the following primary antibodies: β-tubulin Rabbit mAb (A12289, 1:1000 dilution), TGF-β1 Rabbit mAb (ab215715, 1:5000 dilution), and pSmad2/3 mAb (1:1000 dilution). Subsequently, the membranes were incubated with the corresponding HRP-conjugated secondary antibodies at a 1:3000 dilution.

qPCR analysis of PF-related gene after therapy with peptide–si*TGF*-β1 assemblies
The expression levels of fibrosis-related genes in lung tissue after therapy with peptide–si*TGF*-β1 assemblies for 2 weeks were assessed. The total RNA was extracted from snap-frozen lung tissue with TRIzol (no. 15596018, Thermo Fisher Scientific) and quantified using NanoDrop (Thermo Fisher Scientific). mRNA was purified and cDNA was prepared using one NovoScript 1st Strand cDNA Synthesis SuperMix (gDNA Purge) Kit (E047-01B, Novoprotein). Real-time PCR was performed in triplicate using the NovoStart SYBR qPCR SuperMix Plus Kit (E096-01B, Novoprotein) and a Bio-Rad CFX96 real-time PCR system. The relative expression of mRNA was normalized to the expression level of *GAPDH*. The primers of detected genes were listed in table S6.

Histology analysis and immunofluorescence staining
At the end of the treatment with peptide–si*TGF*-β1 assemblies, the mice were euthanized, and lung tissue was collected and fixed with 4% paraformaldehyde. After dehydration, the lung tissue was embedded in paraffin and sectioned for H&E, Masson's trichrome, and PAS staining. For immunofluorescence staining, the lung tissue slides were incubated with sodium citrate antigen retrieval solution (no. C1032, Solarbio) and hydrogen peroxide. After permeabilization and blockage, the lung tissue sections were treated with appropriate primary antibodies. The secondary antibody was applied using Goat Anti-Rabbit IgG H&L (HRP) at 1:1000. Nuclei were stained with DAPI. Immunofluorescence images were captured using a confocal microscope (Leica Stellaris 5) and analyzed by ImageJ software.

Long-term safety evaluation of the consecutive administrations of MNM-siRNA NPs

Eight-week-old C57BL/6J mice received consecutive intratracheal administrations of PBS, naked siRNA, Lipo2000-siRNA, and MNM-siRNA NPs (siRNA 200 μg/kg, 50 μl, N/P = 20) for two consecutive days over a 28-day period. Subsequently, blood samples were collected and analyzed using a Hematology Analyzer to assess white blood cell and RBC parameters. To evaluate lung function, the trachea was exposed by blunt dissection, and an 18G needle was intubated into the trachea and secured with suture. The trachea was then connected to a ventilator, and lung function tests were conducted on day 28 using an invasive, computer-controlled piston ventilator (FlexiVent; SCIREQ Inc.). Furthermore, the major organs were harvested for H&E staining on day 28.

Supplementary Materials
The PDF file includes:
Supplementary Materials and Methods
Figs. S1 to S61
Tables S1 to S8
Legends for movies S1 to S3

Other Supplementary Material for this manuscript includes the following:
Movies S1 to S3

REFERENCES AND NOTES

1. D. J. Lederer, F. J. Martinez, Idiopathic pulmonary fibrosis. *N. Engl. J. Med.* **378**, 1811–1823 (2018).
2. K. H. Shin, S. W. Shin, Idiopathic pulmonary fibrosis. *N. Engl. J. Med.* **379**, 795–796 (2018).
3. P. A. Juge, J. S. Lee, E. Ebstein, H. Furukawa, E. Dobrinskikh, S. Gazal, C. Kannengiesser, S. Ottaviani, S. Oka, S. Tohma, N. Tsuchiya, J. Rojas-Serrano, M. I. Gonzalez-Perez, M. Mejia, I. Buendia-Roldan, R. Falfan-Valencia, E. Ambrocio-Ortiz, E. Manali, S. A. Papiris, T. Karageorgas, D. Boumpas, K. Antoniou, C. H. M. van Moorsel, J. van der Vis, Y. A. de Man, J. C. Grutters, Y. Wang, R. Borie, L. Wemeau-Stervinou, B. Wallaert, R. M. Flipo, H. Nunes, D. Valeyre, N. Saidenberg-Kermanac'h, M. C. Boissier, S. Marchand-Adam, A. Frazier, P. Richette, Y. Allanore, J. Sibilia, C. Dromer, C. Richez, T. Schaeverbeke, H. Lioté, G. Thabut, N. Nathan, S. Amselem, M. Soubrier, V. Cottin, A. Clément, K. Deane, A. D. Walts, T. Fingerlin, A. Fischer, J. H. Ryu, E. L. Matteson, T. B. Niewold, D. Assayag, A. Gross, P. Wolters, M. I. Schwarz, M. Holers, J. J. Solomon, T. Doyle, I. O. Rosas, C. Blauwendraat, M. A. Nalls, M. P. Debray, C. Boileau, B. Crestani, D. A. Schwartz, P. Dieudé, MUC5B promoter variant and rheumatoid arthritis with interstitial lung disease. *N. Engl. J. Med.* **379**, 2209–2219 (2018).
4. F. J. Martinez, H. R. Collard, A. Pardo, G. Raghu, L. Richeldi, M. Selman, J. J. Swigris, H. Taniguchi, A. U. Wells, Idiopathic pulmonary fibrosis. *Nat. Rev. Dis. Primers* **3**, 17074 (2017).
5. F. Karim, J. van Laar, M. van Hagen, Spectrum of fibrotic lung diseases. *N. Engl. J. Med.* **383**, 2485–2486 (2020).
6. L. de Rooij, L. M. Becker, L. A. Teuwen, B. Boeckx, S. Jansen, S. Feys, S. Verleden, L. Liesenborghs, A. K. Stalder, S. Libbrecht, T. Van Buyten, G. Philips, A. Subramanian, S. J. Dumas, E. Meta, M. Borri, L. Sokol, A. Dendooven, A. C. K. Truong, J. Gunst, P. Van Mol, J. D. Haslbauer, K. Rohlenova, T. Menter, R. Boudewijns, V. Geldhof, S. Vinckier, J. Amersfoort, W. Wuyts, D. Van Raemdonck, W. Jacobs, J. Ceulemans, B. Weynand, B. Thienpont, M. Lammens, M. Kuehnel, G. Eelen, M. Dewerchin, L. Schoonjans, D. Jonigk, J. van Dorpe, A. Tzankov, E. Wauters, M. Mazzone, J. Neyts, J. Wauters, D. Lambrechts, P. Carmeliet, The pulmonary vasculature in lethal COVID-19 and idiopathic pulmonary fibrosis at single-cell resolution. *Cardiovasc. Res.* **119**, 520–535 (2023).
7. V. J. Thannickal, G. B. Toews, E. S. White, J. P. Lynch, F. J. Martinez, Mechanisms of pulmonary fibrosis. *Annu. Rev. Med.* **55**, 395–417 (2004).
8. T. Fabre, A. M. S. Barron, S. M. Christensen, S. Asano, K. Bound, M. P. Lech, M. H. Wadsworth, X. Chen, C. Wang, J. Wang, J. McMahon, F. Schlerman, A. White, K. M. Kravarik, A. J. Fisher, L. A. Borthwick, K. M. Hart, N. C. Henderson, T. A. Wynn, K. Dower, Identification of a broadly fibrogenic macrophage subset induced by type 3 inflammation. *Sci. Immunol.* **8**, add8945 (2023).
9. M. Kolb, G. Raghu, A. U. Wells, J. Behr, L. Richeldi, B. Schinzel, M. Quaresma, S. Stowasser, F. J. Martinez, I. Investigators, Nintedanib plus Sildenafil in patients with idiopathic pulmonary fibrosis. *N. Engl. J. Med.* **379**, 1722–1731 (2018).
10. L. Richeldi, H. R. Collard, M. G. Jones, Idiopathic pulmonary fibrosis. *Lancet* **389**, 1941–1952 (2017).
11. A. K. Patel, J. C. Kaczmarek, S. Bose, K. J. Kauffman, F. Mir, M. W. Heartlein, F. DeRosa, R. Langer, D. G. Anderson, Inhaled nanoformulated mRNA polyplexes for protein production in lung epithelium. *Adv. Mater.* **31**, e1805116 (2019).
12. A. S. Piotrowski-Daspit, C. Barone, C. Y. Lin, Y. X. Deng, D. G. Wu, T. C. Binns, E. M. Y. Xu, A. S. Ricciardi, R. Putman, A. Garrison, R. Nguyen, A. Gupta, R. Fan, P. M. Glazer, W. M. Saltzman, M. E. Egan, In vivo correction of cystic fibrosis mediated by PNA nanoparticles. *Sci. Adv.* **8**, eabo0522 (2022).
13. Q. J. Ji, J. W. Hou, X. Q. Yong, G. M. Gong, M. Muddassir, T. Y. Tang, J. B. Xie, W. P. Fan, X. Y. Chen, Targeted dual small interfering ribonucleic acid delivery via non-viral polymeric vectors for pulmonary fibrosis therapy. *Adv. Mater.* **33**, e2007798 (2021).
14. X. Bai, G. L. Zhao, Q. J. Chen, Z. Y. Li, M. Z. Gao, W. Ho, X. Y. Xu, X. Q. Zhang, Inhaled siRNA nanoparticles targeting IL11 inhibit lung fibrosis and improve pulmonary function post-bleomycin challenge. *Sci. Adv.* **8**, eabn7162 (2022).
15. D. D. Peng, M. Y. Fu, M. N. Wang, Y. Q. Wei, X. W. Wei, Targeting TGF-β signal transduction for fibrosis and cancer therapy. *Mol. Cancer* **21**, 104 (2022).
16. Y. Zhuo, Z. Luo, Z. Zhu, J. Wang, X. Li, Z. Zhang, C. Guo, B. Wang, D. Nie, Y. Gan, G. Hu, M. Yu, Direct cytosolic delivery of siRNA via cell membrane fusion using cholesterol-enriched exosomes. *Nat. Nanotechnol.* **19**, 1858–1868 (2024).
17. G. A. Duncan, J. Jung, J. Hanes, J. S. Suk, The mucus barrier to inhaled gene therapy. *Mol. Ther.* **24**, 2043–2053 (2016).
18. B. Button, L. H. Cai, C. Ehre, M. Kesimer, D. B. Hill, J. K. Sheehan, R. C. Boucher, M. Rubinstein, A periciliary brush promotes the lung health by separating the mucus layer from airway epithelia. *Science* **337**, 937–941 (2012).
19. S. Yuan, M. Hollinger, M. E. Lachowicz-Scroggins, S. C. Kerr, E. M. Dunican, B. M. Daniel, S. Ghosh, S. C. Erzurum, B. Willard, S. L. Hazen, X. Z. Huang, S. D. Carrington, S. Oscarson, J. V. Fahy, Oxidation increases mucin polymer cross-links to stiffen airway mucus gels. *Sci. Transl. Med.* **7**, 276ra227 (2015).
20. N. Kim, G. A. Duncan, J. Hanes, J. S. Suk, Barriers to inhaled gene therapy of obstructive lung diseases: A review. *J. Control. Release* **240**, 465–488 (2016).
21. D. Chen, N. Kong, H. Wang, Leading-edge pulmonary gene therapy approached by barrier-permeable delivery system: A concise review on peptide system. *Adv. NanoBiomed Res.* **2**, 202200113 (2022).
22. G. Alp, N. Aydogan, Lipid-based mucus penetrating nanoparticles and their biophysical interactions with pulmonary mucus layer. *Eur. J. Pharm. Biopharm.* **149**, 45–57 (2020).
23. C. L. Ge, J. D. Yang, S. Z. Duan, Y. Liu, F. H. Meng, L. C. Yin, Fluorinated α-helical polypeptides synchronize mucus permeation and cell penetration toward highly efficient pulmonary siRNA delivery against acute lung injury. *Nano Lett.* **20**, 1738–1746 (2020).
24. Z. X. Wang, J. X. Zhang, Y. F. Wang, J. L. Zhou, X. H. Jiao, M. S. Han, X. L. Zhang, H. L. Hu, R. X. Su, Y. M. Zhang, W. Qi, Overcoming endosomal escape barriers in gene drug delivery using de novo designed pH-responsive peptides. *ACS Nano* **18**, 10324–10340 (2024).
25. A. Y. Jiang, J. Witten, I. O. Raji, F. Eweje, C. Macisaac, S. Meng, F. A. Oladimeji, Y. Z. Hu, R. S. Manan, R. Langer, D. G. Anderson, Combinatorial development of nebulized mRNA delivery formulations for the lungs. *Nat. Nanotechnol.* **19**, 364–375 (2024).
26. X. Bai, Q. J. Chen, F. Q. Li, Y. L. Teng, M. P. Tang, J. Huang, X. Y. Xu, X. Q. Zhang, Optimized inhaled LNP formulation for enhanced treatment of idiopathic pulmonary fibrosis via mRNA-mediated antibody therapy. *Nat. Commun.* **15**, 6844 (2024).
27. M. R. Liu, S. Q. Hu, N. Yan, K. D. Popowski, K. Cheng, Inhalable extracellular vesicle delivery of IL-12 mRNA to treat lung cancer and promote systemic immunity. *Nat. Nanotechnol.* **19**, 565–575 (2024).
28. S. Guan, A. Munder, S. Hedtfeld, P. Braubach, S. Glage, L. G. Zhang, S. Lienenklaus, A. Schultze, G. Hasenpusch, W. Garrels, F. Stanke, C. Miskey, S. M. Johler, Y. Kumar, B. Tümmler, C. Rudolph, Z. Ivics, J. Rosenecker, Self-assembled peptide-poloxamine nanoparticles enable in vitro and in vivo genome restoration for cystic fibrosis. *Nat. Nanotechnol.* **14**, 287–297 (2019).
29. Q. Cheng, T. Wei, L. Farbiak, L. T. Johnson, S. A. Dilliard, D. J. Siegwart, Selective organ targeting (SORT) nanoparticles for tissue-specific mRNA delivery and CRISPR-Cas gene editing. *Nat. Nanotechnol.* **15**, 313–320 (2020).
30. Y. Wang, J. Zhang, Y. Liu, X. Yue, K. Han, Z. C. Kong, Y. M. Dong, Z. M. Yang, Z. P. Fu, C. W. Tang, C. D. Shi, X. T. Zhao, M. S. Han, Z. B. Wang, Y. L. Zhang, C. Chen, A. N. Li, P. Sun, D. Q. Zhu, K. Zhao, X. Y. Jiang, Realveolarization with inhalable mucus-penetrating lipid nanoparticles for the treatment of pulmonary fibrosis in mice. *Sci. Adv.* **10**, eado4791 (2024).
31. C. Wilson, Future therapies for cystic fibrosis. *Lancet Respir. Med.* **10**, E75 (2022).
32. S. M. Rowe, J. B. Zuckerman, D. Dorgan, J. Lascano, K. Mccoy, M. Jain, M. S. Schechter, S. Lommatzsch, V. Indihar, N. Lechtzin, K. McBennett, C. Callison, C. Brown, T. G. Liou, K. D. MacDonald, S. Z. Nasr, S. Bodie, M. Vaughn, E. B. Meltzer, A. J. Barbier, Inhaled mRNA therapy for treatment of cystic fibrosis: Interim results of a randomized, double-blind, placebo-controlled phase 1/2 clinical study. *J. Cystic Fibrosis* **22**, 656–664 (2023).
33. M. Beck-Broichsitter, O. M. Merkel, T. Kissel, Controlled pulmonary drug and gene delivery using polymeric nano-carriers. *J. Control. Release* **161**, 214–224 (2012).
34. B. W. Li, R. S. Manan, S. Q. Liang, A. Gordon, A. L. Jiang, A. Varley, G. P. Gao, R. Langer, W. Xue, D. Anderson, Combinatorial design of nanoparticles for pulmonary mRNA delivery and genome editing. *Nat. Biotechnol.* **41**, 1410–1415 (2023).

35. S. Krishnamurthy, C. Wohlford-Lenane, S. Kandimalla, G. Sartre, D. K. Meyerholz, V. Théberge, S. Hallée, A.-M. Duperré, T. Del'Guidice, J.-P. Lepetit-Stoffaes, X. Barbeau, D. Guay, P. B. McCray, Engineered amphiphilic peptides enable delivery of proteins and CRISPR-associated nucleases to airway epithelia. *Nat. Commun.* **10**, 4906 (2019).

36. P. Majumder, A. Singh, Z. Q. Wang, K. Dutta, R. Pahwa, C. Liang, C. Andrews, N. L. Patel, J. F. Shi, N. de Val, S. T. R. Walsh, A. B. Jeon, B. Karim, C. D. Hoang, J. P. Schneider, Surface-fill hydrogel attenuates the oncogenic signature of complex anatomical surface cancer in a single application. *Nat. Nanotechnol.* **16**, 1251–1259 (2021).

37. H. M. Wang, Z. Feng, B. Xu, Supramolecular assemblies of peptides or nucleopeptides for gene delivery. *Theranostics* **9**, 3213–3222 (2019).

38. L. C. Yin, J. J. Cheng, T. J. Deming, M. J. Vicent, Synthetic polypeptides for drug and gene delivery, and tissue engineering. *Adv. Drug Del. Rev.* **178**, 113995 (2021).

39. J. Q. Guo, F. B. Wang, Y. M. Huang, H. J. He, W. Y. Tan, M. H. Yi, E. H. Egelman, B. Xu, Cell spheroid creation by transcytotic intercellular gelation. *Nat. Nanotechnol.* **18**, 1094–1104 (2023).

40. S. S. Lee, T. Fyrner, F. Chen, Z. Alvarez, E. Sleep, D. S. Chun, J. A. Weiner, R. W. Cook, R. D. Freshman, M. S. Schallmo, K. M. Katchko, A. D. Schneider, J. T. Smith, C. W. Yun, G. Singh, S. Z. Hashmi, M. T. McClendon, Z. L. Yu, S. R. Stock, W. K. Hsu, E. L. Hsu, S. I. Stupp, Sulfated glycopeptide nanostructures for multipotent protein activation. *Nat. Nanotechnol.* **12**, 821–829 (2017).

41. S. G. Zhang, Fabrication of novel biomaterials through molecular self-assembly. *Nat. Biotechnol.* **21**, 1171–1178 (2003).

42. E. Gazit, Self-assembled peptide nanostructures: The design of molecular building blocks and their technological utilization. *Chem. Soc. Rev.* **36**, 1263–1269 (2007).

43. J. W. Yoo, D. J. Irvine, D. E. Discher, S. Mitragotri, Bio-inspired, bioengineered and biomimetic drug delivery carriers. *Nat. Rev. Drug Discov.* **10**, 521–535 (2011).

44. S. Ling, X. Zhang, Y. Dai, Z. Jiang, X. Zhou, S. Lu, X. Qian, J. Liu, N. Selfjord, T. M. Satir, A. Lundin, J. L. Touza, M. Firth, N. Van Zuydam, B. Bilican, P. Akcakaya, J. Hong, Y. Cai, Customizable virus-like particles deliver CRISPR-Cas9 ribonucleoprotein for effective ocular neovascular and Huntington's disease gene therapy. *Nat. Nanotechnol.* **20**, 543–553 (2025).

45. S. Banskota, A. Raguram, S. Suh, S. W. Du, J. R. Davis, E. H. Choi, X. Wang, S. C. Nielsen, G. A. Newby, P. B. Randolph, M. J. Osborn, K. Musunuru, K. Palczewski, D. R. Liu, Engineered virus-like particles for efficient in vivo delivery of therapeutic proteins. *Cell* **185**, 250–265.e16 (2022).

46. G. L. Butterfield, M. J. Lajoie, H. H. Gustafson, D. L. Sellers, U. Nattermann, D. Ellis, J. B. Bale, S. Ke, G. H. Lenz, A. Yehdego, R. Ravichandran, S. H. Pun, N. P. King, D. Baker, Evolution of a designed protein assembly encapsulating its own RNA genome. *Nature* **552**, 415–420 (2017).

47. D. Strebinger, C. J. Frangieh, M. J. Friedrich, G. Faure, R. K. Macrae, F. Zhang, Cell type-specific delivery by modular envelope design. *Nat. Commun.* **14**, 5141 (2023).

48. A. Komin, L. M. Russell, K. A. Hristova, P. C. Searson, Peptide-based strategies for enhanced cell uptake, transcellular transport, and circulation: Mechanisms and challenges. *Adv. Drug Del. Rev.* **110**, 52–64 (2017).

49. K. Luger, A. W. Mäder, R. K. Richmond, D. F. Sargent, T. J. Richmond, Crystal structure of the nucleosome core particle at 2.8 Å resolution. *Nature* **389**, 251–260 (1997).

50. G. A. Armeev, A. S. Kniazeva, G. A. Komarova, M. P. Kirpichnikov, A. K. Shaytan, Histone dynamics mediate DNA unwrapping and sliding in nucleosomes. *Nat. Commun.* **12**, 2387 (2021).

51. J. Leal, X. J. Peng, X. Q. Liu, D. Arasappan, D. C. Wylie, S. H. Schwartz, J. J. Fullmer, B. C. McWilliams, H. D. C. Smyth, D. Ghosh, Peptides as surface coatings of nanoparticles that penetrate human cystic fibrosis sputum and uniformly distribute in vivo following pulmonary delivery. *J. Control. Release* **322**, 457–469 (2020).

52. J. Leal, T. Dong, A. Taylor, E. Siegrist, F. Gao, H. D. C. Smyth, D. Ghosh, Mucus-penetrating phage-displayed peptides for improved transport across a mucus-like model. *Int. J. Pharm.* **553**, 57–64 (2018).

53. J. L. Huang, G. Jiang, Q. X. Song, X. Gu, M. Hu, X. L. Wang, H. H. Song, L. P. Chen, Y. Y. Lin, D. Jiang, J. Chen, J. F. Feng, Y. M. Qiu, J. Y. Jiang, X. G. Jiang, H. Z. Chen, X. L. Gao, Lipoprotein-biomimetic nanostructure enables efficient targeting delivery of siRNA to Ras-activated glioblastoma cells via macropinocytosis. *Nat. Commun.* **8**, 15144 (2017).

54. J. J. Rennick, A. P. R. Johnston, R. G. Parton, Key principles and methods for studying the endocytosis of biological and nanoparticle therapeutics. *Nat. Nanotechnol.* **16**, 266–276 (2021).

55. J. S. Suk, A. J. Kim, K. Trehan, C. S. Schneider, L. Cebotaru, O. M. Woodward, N. J. Boylan, M. P. Boyle, S. K. Lai, W. B. Guggino, J. Hanes, Lung gene therapy with highly compacted DNA nanoparticles that overcome the mucus barrier. *J. Control. Release* **178**, 8–17 (2014).

56. S. Koo, H. S. Sohn, T. H. Kim, S. Yang, S. Y. Jang, S. Ye, B. Choi, S. H. Kim, K. S. Park, H. M. Shin, O. K. Park, C. Kim, M. Kang, M. Soh, J. Yoo, D. Kim, N. Lee, B. S. Kim, Y. Jung, T. Hyeon, Ceria-vesicle nanohybrid therapeutic for modulation of innate and adaptive immunity in a collagen-induced arthritis model. *Nat. Nanotechnol.* **18**, 1502–1514 (2023).

57. Z. J. Li, L. Amaya, A. Ee, S. K. Wang, A. Ranjan, R. M. Waymouth, H. Y. Chang, P. A. Wender, Organ- and cell-selective delivery of mRNA in vivo using guanidinylated serinol charge-altering releasable transporters. *J. Am. Chem. Soc.* **146**, 14785–14798 (2024).

58. F. Eweje, V. Ibrahim, A. Shajii, M. L. Walsh, K. Ahmad, A. Alrefai, D. Miyasato, J. R. Davis, H. Ham, K. C. Li, M. Roehrl, C. A. Haller, D. R. Liu, J. X. Chen, E. L. Chaikof, Self-assembling protein nanoparticles for cytosolic delivery of nucleic acids and proteins. *Nat. Biotechnol.* **43**, DOI: 10.1038/s41587-025-02664-2 (2025).

59. C. I. Grainger, L. L. Greenwell, D. J. Lockley, G. P. Martin, B. Forbes, Culture of Calu-3 cells at the air interface provides a representative model of the airway epithelial barrier. *Pharm. Res.* **23**, 1482–1490 (2006).

60. J. S. Suk, S. K. Lai, Y. Y. Wang, L. M. Ensign, P. L. Zeitlin, M. P. Boyle, J. Hanes, The penetration of fresh undiluted sputum expectorated by cystic fibrosis patients by non-adhesive polymer nanoparticles. *Biomaterials* **30**, 2591–2597 (2009).

61. M. L. Cohen, A. N. Brumwell, T. C. Ho, K. Garakani, G. Montas, D. Leong, V. W. Ding, J. A. Golden, B. N. Trinh, D. M. Jablons, M. A. Matthay, K. D. Jones, P. J. Wolters, Y. Wei, H. A. Chapman, C. J. Le Saux, A fibroblast-dependent TGF-β1/sFRP2 noncanonical Wnt signaling axis promotes epithelial metaplasia in idiopathic pulmonary fibrosis. *J. Clin. Invest.* **134**, e174598 (2024).

62. S. Y. Gao, X. H. Li, Q. Y. Jiang, Q. Liang, F. X. Zhang, S. L. Li, R. Q. Zhang, J. Y. Luan, J. Y. Zhu, X. T. Gu, T. Xiao, H. Huang, S. S. Chen, W. Ning, G. Yang, C. Yang, H. G. Zhou, PKM2 promotes pulmonary fibrosis by stabilizing TGF-β1 receptor I and enhancing TGF-β1 signaling. *Sci. Adv.* **8**, eabo0987 (2022).

63. M. J. Hao, Z. J. Guan, Z. K. Zhang, H. P. Ai, X. Peng, H. H. Zhou, J. Xu, Q. Gu, Atractylodinol prevents pulmonary fibrosis through inhibiting TGF-β receptor 1 recycling by stabilizing vimentin. *Mol. Ther.* **31**, 3015–3033 (2023).

64. D. Bouros, Pirfenidone for idiopathic pulmonary fibrosis. *Lancet* **377**, 1727–1729 (2011).

65. V. Cottin, Treatment of progressive fibrosing interstitial lung diseases: A milestone in the management of interstitial lung diseases. *Eur. Respir. Rev.* **28**, 190109 (2019).